



## Sea ice dynamics in the Bransfield Strait, Antarctic Peninsula, during the past 240 years: a multi-proxy intercomparison study

Maria-Elena Vorrath<sup>1</sup>, Juliane Müller<sup>1,2,3</sup>, Lorena Rebolledo<sup>4,5</sup>, Paola Cárdenas<sup>4</sup>, Xiaoxu Shi<sup>1</sup>, Oliver Esper<sup>1</sup>, Thomas Opel<sup>1</sup>, Walter Geibert<sup>1</sup>, Práxedes Muñoz<sup>6</sup>, Christian Haas<sup>1</sup>, Gerhard Kuhn<sup>1</sup>, Carina B. Lange<sup>4,7,8,9</sup>, Gerrit Lohmann<sup>1</sup>, and Gesine Mollenhauer<sup>1,2</sup>

<sup>1</sup>Alfred Wegener Institute, Helmholtz Centre for Polar and Marine Research, Bremerhaven, Germany

<sup>2</sup>MARUM – Center for Marine Environmental Sciences, University of Bremen, Bremen, Germany

<sup>3</sup>Department of Geosciences, University of Bremen, Germany

<sup>4</sup>Centro de Investigación Dinámica de Ecosistemas Marinos de Altas Latitudes (IDEAL), Universidad Austral de Chile, Valdivia, Chile

<sup>5</sup>Instituto Antártico Chileno (INACH), Punta Arenas, Chile

<sup>6</sup>Facultad de Ciencias del Mar, Universidad Católica del Norte, Coquimbo, Chile

<sup>7</sup>Centro Oceanográfico COPAS Sur-Austral, Universidad de Concepción, Concepción, Chile

<sup>8</sup>Departamento de Oceanografía, Universidad de Concepción, Chile

<sup>9</sup>Scripps Institution of Oceanography, La Jolla, CA 92037, USA

**Correspondence:** Maria-Elena Vorrath (maria-elena.vorrath@awi.de)

Received: 4 May 2020 – Discussion started: 12 May 2020

Revised: 22 October 2020 – Accepted: 23 October 2020 – Published: 11 December 2020

**Abstract.** In the last decades, changing climate conditions have had a severe impact on sea ice at the western Antarctic Peninsula (WAP), an area rapidly transforming under global warming. To study the development of spring sea ice and environmental conditions in the pre-satellite era we investigated three short marine sediment cores for their biomarker inventory with a particular focus on the sea ice proxy IPSO<sub>25</sub> and micropaleontological proxies. The core sites are located in the Bransfield Strait in shelf to deep basin areas characterized by a complex oceanographic frontal system, coastal influence and sensitivity to large-scale atmospheric circulation patterns. We analyzed geochemical bulk parameters, biomarkers (highly branched isoprenoids, glycerol dialkyl glycerol tetraethers, sterols), and diatom abundances and diversity over the past 240 years and compared them to observational data, sedimentary and ice core climate archives, and results from numerical models. Based on biomarker results we identified four different environmental units characterized by (A) low sea ice cover and high ocean temperatures, (B) moderate sea ice cover with decreasing ocean temperatures, (C) high but variable sea ice cover during intervals of lower ocean temperatures, and (D) extended sea ice

cover coincident with a rapid ocean warming. While IPSO<sub>25</sub> concentrations correspond quite well to satellite sea ice observations for the past 40 years, we note discrepancies between the biomarker-based sea ice estimates, the long-term model output for the past 240 years, ice core records, and reconstructed atmospheric circulation patterns such as the El Niño–Southern Oscillation (ENSO) and Southern Annular Mode (SAM). We propose that the sea ice biomarker proxies IPSO<sub>25</sub> and PIPSO<sub>25</sub> are not linearly related to sea ice cover, and, additionally, each core site reflects specific local environmental conditions. High IPSO<sub>25</sub> and PIPSO<sub>25</sub> values may not be directly interpreted as referring to high spring sea ice cover because variable sea ice conditions and enhanced nutrient supply may affect the production of both the sea-ice-associated and phytoplankton-derived (open marine, pelagic) biomarker lipids. For future interpretations we recommend carefully considering individual biomarker records to distinguish between cold sea-ice-favoring and warm sea-ice-diminishing environmental conditions.

## 1 Introduction

Observations of global mean surface temperatures show a warming of approximately  $1.0 \pm 0.2$  °C (IPCC, 2018) above the 1850–1900 baseline as a result of progressive industrialization since the mid-19th century. An acceleration of this trend due to anthropogenic forcing has been projected (IPCC, 2019). The ocean, especially the Southern Ocean, takes up the majority of the atmospheric heat, and warming has already been observed at all depths (IPCC, 2019). Antarctica's hot spot of warming is the western Antarctic Peninsula (WAP) (Jones et al., 2016) with an atmospheric temperature increase of  $3.7 \pm 1.6$  °C in the 20th century (Vaughan et al., 2003) and a slight cooling from 2000 to 2010 (Turner et al., 2019). From the 1990s to 2000s, a warming of up to 1 °C of subsurface water is also evident in different water masses around the WAP (Cook et al., 2016). On land, glaciers and ice shelves on both sides of the Antarctic Peninsula (AP) have retreated rapidly since the 2000s (Cook et al., 2016; Rignot et al., 2019), pointing towards a potential collapse of the WAP ice shelves, while the loss of sea ice cover is also significant (Parkinson and Cavalieri, 2012). Shortened sea ice seasons (Parkinson, 2002) and a reduction of sea ice extent accelerating from 4 % up to 10 % per decade (Liu et al., 2004) have been observed in the region via satellite since 1979. A recent compilation shows that the steady increase in sea ice extent around the entire Antarctic continent since 1979 stopped in 2014 and was followed by fast decreases (Parkinson, 2019). However, the region along the WAP, the Bellingshausen Sea and Amundsen Sea shows contrasting sea ice trends and high sea ice variability in 2014 and afterwards (Hobbs et al., 2016). The changes in sea ice cover are not only related to warm water intrusion and higher sea surface temperatures (SSTs) along the WAP (Martinson and McKee, 2012; Meredith and King, 2005), but also to large-scale modes of atmospheric circulation such as the Southern Annular Mode (SAM) (e.g., Barbara et al., 2013) and the El Niño–Southern Oscillation (ENSO) (e.g., Liu et al., 2004) or a combination of both (Etourneau et al., 2013; Stammerjohn et al., 2008b, a).

Sea ice is an important factor that shapes and influences the Southern Ocean. Melting sea ice releases nutrients and leads to enhanced primary production and ocean stratification during spring and summer (Arrigo et al., 1997; Vernet et al., 2008). Interestingly, a higher number of sea ice days is associated with increased photosynthetic efficiency and enhanced carbon fixation rates due to greater nutrient delivery stimulating primary production (Schofield et al., 2018), but thinning of sea ice also affects marine productivity positively (Hancke et al., 2018). Release of dense brine during sea ice formation leads to water mass transformations (Abernathy et al., 2016) that contribute to the thermohaline circulation by feeding deep and intermediate waters (Nicholls et al., 2009) and at the same time inducing upwelling at sea ice edges (Alexander and Niebauer, 1981). Sea ice cover also reduces

the ocean–atmosphere exchange of heat and gases as well as regional precipitation, enhances the albedo (Allison et al., 1982; Butterworth and Miller, 2016; Turner et al., 2017), and is a potential source of the radiative-relevant volatile dimethylsulfide produced by phytoplankton (Trevena and Jones, 2006) – a precursor of methanesulfonic acid (MSA) (Abram et al., 2010). Sea ice changes along the WAP may lead to the destabilization and/or collapse of local ice shelves due to warm water intrusions and basal melting (Cook et al., 2016; Etourneau et al., 2019; Hellmer et al., 2012), promoting an accelerated ice sheet flow towards the ocean (Huss and Farinotti, 2014). Sea ice decline in this region may thus also indirectly contribute to global sea level rise.

Atmospheric circulation patterns such as ENSO and SAM have been suggested to control SST and the distribution of sea ice along the WAP (Ding et al., 2012; Stammerjohn et al., 2008b, 2008a). Etourneau et al. (2013) concluded from the occurrence of higher sea ice cover together with higher SSTs that a rising number of ENSO events would increase the seasonal amplitude of warmer summers and colder winters in the region. SAM is the leading climate mode in the Southern Hemisphere (Jones et al., 2016) and has significant impacts on temperatures at the northeast AP (Clem et al., 2016). Stammerjohn et al. (2008b) link ENSO- and SAM-related teleconnections to opposite sea ice trends in the Pacific and Atlantic sector of the Southern Ocean on decadal scales during the satellite era. The high-latitude responses and ice–atmosphere anomalies are strongest when a positive ENSO occurs “in phase” with a negative SAM (+ENSO/−SAM) and the subtropical jet over the Pacific Ocean is strengthened, whereas the polar frontal jet and the westerly winds are weaker (Stammerjohn et al., 2008b). In this state, a positive sea level pressure establishes a high-pressure cell in the Pacific Southern Ocean and warmer, moister conditions with less sea ice are established there. Meanwhile, the Weddell Sea and the WAP experience a cooling with an advance of sea ice. During the opposite state (−ENSO/+SAM) a stronger polar frontal jet establishes a low-pressure cell in the Bellingshausen Sea. In this case, increased southward-migrated westerly winds transport heat towards the WAP and the Weddell Sea, and sea ice cover is reduced under high atmospheric and sea surface temperatures (Marshall et al., 2006; Stammerjohn et al., 2008b; Yuan, 2004). Clem et al. (2016) propose that the combined effect of in-phase ENSO and SAM is strongest in spring. A positive SAM reduces the interaction of water masses between the Bransfield Strait and the Weddell Sea, whereas higher Weddell Sea Water (WSW) input occurs during a negative SAM due to the northward shift of the wind belt and ocean fronts and stronger coastal currents in the Weddell Sea (Dotto et al., 2016).

For modeling past and future Antarctic climate, ice sheet stability, the thermohaline circulation, or the impacts of sea ice loss for ecosystems, data on past sea ice cover are crucial although barely available (Bracegirdle et al., 2015, 2019). For the WAP, insights into climate and sea ice dynamics

during the past 200 years are available from ice cores (stable isotopes, marine aerosols and snow accumulation), but information from high-resolution marine sediments and in particular sedimentary, geochemical or diatom-based sea ice proxies remains sparse (Thomas et al., 2019). Sinking marine particles carry environmental information from the sea surface to the ocean floor, and, when buried in the sediments, the environmental history including sea ice can be deduced from these marine climate archives. For sea ice reconstructions, the use of sea-ice-associated diatom species and biogeochemical parameters is common (Crosta et al., 1998; Esper and Gersonde, 2014a; Gersonde and Zielinski, 2000). Since diatom frustules may be affected by the dissolution of biogenic opal in the photic zone (Ragueneau et al., 2000), on the ocean floor (Leventer, 1998) and in the sediments (Burckle and Cooke, 1983; Esper and Gersonde, 2014b), increasing attention is paid to their molecular remains, i.e., specific biomarker lipids, as promising tools for past sea ice reconstructions (Massé et al., 2011). A specific di-unsaturated highly branched isoprenoid alkene (HBI diene, C<sub>25:2</sub>) has been proposed as a potential tool for past spring sea ice reconstructions in the Southern Ocean (Massé et al., 2011). It is produced by sea ice diatoms (Nichols et al., 1988) and its sea ice origin is evident from the high  $\delta^{13}\text{C}$  isotopic signature of the molecule (Massé et al., 2011; Sinninghe Damsté et al., 2007; Vorrath et al., 2019). The sea ice diatom *Berkeleya adeliensis*, which is observed to mainly occur during spring in Antarctic landfast ice and platelet ice (Riaux-Gobin and Poulin, 2004), was identified as a producer of the HBI diene (Belt et al., 2016). The HBI diene is present in surface and downcore sediments around Antarctica and – in analogy to the Arctic IP<sub>25</sub> – can be used as an IPSO<sub>25</sub> (ice proxy for the Southern Ocean with 25 carbon atoms), likely showing the extent of near-coastal spring sea ice (Belt et al., 2016; Lamping et al., 2020; Massé et al., 2011; Riaux-Gobin and Poulin, 2004; Vorrath et al., 2019). To differentiate between an extended spring sea ice cover, the occurrence of a stable sea ice margin and/or an open marine environment, IPSO<sub>25</sub> is combined with phytoplankton-derived biomarker lipids such as HBI trienes and/or sterols, which are considered proxies for open water conditions (Belt and Müller, 2013; Volkman, 1986). Analogous to the PIP<sub>25</sub> index (P indicates an open marine phytoplankton marker) for semi-quantitative sea ice estimations in the Arctic (Müller et al., 2011), the recently proposed PIPSO<sub>25</sub> approach (Vorrath et al., 2019) allows for a differentiation between several sea ice conditions of a permanently open ocean, a sea ice marginal zone and a permanent sea ice cover.

Here, we provide the first IPSO<sub>25</sub>-based high-resolution assessment of the spring sea ice development in the Bransfield Strait during the past 240 years and examine the response of sea ice to changes in atmospheric and oceanic oscillation patterns. To achieve this, we conducted a multi-proxy study on three short sediment cores retrieved from different oceanic regimes to cover regional differences within

the Bransfield Strait. In addition to IPSO<sub>25</sub>, we analyzed HBI trienes, sterols and glycerol dialkyl glycerol tetraethers (GDGTs) for subsurface ocean temperature (SOT) reconstruction as well as diatom assemblages for estimating winter sea ice (WSI) concentrations and summer sea surface temperatures (SSSTs) by means of transfer functions. We furthermore consider sea ice and temperature data from an atmosphere–sea ice–ocean numerical model (AWI-ESM2), historical surface air temperatures from local meteorological stations, ice core records (stable isotopes  $\delta^{18}\text{O}$  and  $\delta\text{D}$ , MSA, annual net snow accumulation  $A_n$ ), and paleo-records of atmospheric circulation patterns such as ENSO and SAM.

## 2 Material and methods

### 2.1 Study area

The study area is the Bransfield Strait at the northern tip of the WAP (Fig. 1a and b). The region includes the shallow shelf of the WAP and the Bransfield Basin with depths exceeding 2000 m at its deepest parts. The Bransfield Basin is located between the South Shetland Islands (SSI) to the northwest and the AP to the southeast. The shallow ocean has been shaped by ice sheet dynamics during the last glaciation (Canals and Amblas, 2016b; Ingólfsson et al., 2003), and several troughs discharge sediment load from the AP and SSI into the basin (Canals et al., 2016; Canals and Amblas, 2016a). The oceanographic setting in this area is complex and not yet fully constrained (Moffat and Meredith, 2018; Sangrà et al., 2011) because water masses enter the basin from the west and east (Fig. 1b). From the east, relatively cold ( $< 0^\circ\text{C}$ ) and salty WSW flows at the surface along the shore of the AP as a coastal current but also fills the Bransfield Basin completely below 150 m. It is also observed on the northern slope of the SSI at 200–600 m of depth and around Elephant Island as a result of wind-driven modulation (Meijers et al., 2016). The main water source from the west is the Bellingshausen Sea Water (BSW) transported by the Antarctic Circumpolar Current (ACC). This well-stratified, fresh and warm surface water flows along the slope of the SSI and forms the Peninsula Front with the WSW in the central Bransfield Strait, trending southwest–northeast parallel to the AP (Sangrà et al., 2011). Additionally, Circumpolar Deep Water (CDW) enters from the southwest as a subsurface current, forming the Bransfield Front to the BSW at 200 to 550 m of depth along the SSI slope (Sangrà et al., 2017). Both BSW and CDW are observed to turn and flow back at the northern side of the SSI (Sangrà et al., 2011). The mixing and transformation of the three water masses in the Bransfield Strait is yet not well understood, but a study of iceberg drifts from Collares et al. (2018) showed that water from the Weddell Sea join waters from the Bellingshausen Sea in the vicinity of Trinity Island (Fig. 1b). The input of WSW is suggested to be enhanced by a strong Weddell Gyre during a negative SAM and diminished during a positive SAM (Dotto

et al., 2016). In the Bransfield Strait it has been suggested that eddies between the Peninsula Front and the Bransfield Front are a key mechanism for water exchange and/or upwelling (Sangrà et al., 2011; Zhou et al., 2002), and melt-water discharge from the adjacent glaciers has to be considered (Meredith et al., 2018). In the southwest, south of the Bransfield Strait, a narrow, fast-flowing Antarctic Peninsula Coastal Current (APCC) is present, enriched in glacial fresh water and characterized by downwelling (Moffat and Meredith, 2018). The APCC surface water flows northward and southward of Anvers Island are significantly reduced during sea ice cover (Moffat and Meredith, 2018).

Primary productivity along the WAP is mainly controlled by eddies and fronts (Gonçalves-Araujo et al., 2015) due to upwelling (Sangrà et al., 2011), sea ice dynamics (Vernet et al., 2008) and iron distribution (Klunder et al., 2014). Diatom-associated high-productivity regimes and high chlorophyll concentrations are found north of the Peninsula Front along the SSI under the influence of the BSW, while the area influenced by the WSW is characterized by lower production of nanoplankton (Gonçalves-Araujo et al., 2015). Heterogeneous upwelling, iron fertilization and sea ice retreat lead to high interannual variability in the production patterns, and a strong onshore–offshore gradient is evident. In consequence high production is related to coastal areas, shallow mixed layers and higher stratification owing to sea ice melting (Sanchez et al., 2019; Vernet et al., 2008). High primary production is also reflected in high vertical export of sinking particles (e.g., Wefer et al., 1988; Kim et al., 2004) and in the biogeochemical distribution of surface sediments, dominated by high concentrations of total organic carbon (TOC), pigments, sterols and diatoms but low calcium carbonate (Cárdenas et al., 2019). Organic matter is mainly of marine origin as supported by low values of C/N and the stable carbon isotope composition (Cárdenas et al., 2019), whereas the AP is an important source of terrestrial silts and clays (Wu et al., 2019).

## 2.2 Sampling and age model

The cores were collected in 2016 during the RV *Polarstern* cruise PS97 (ANT-XXXI/3) using a multicorer at stations PS97/056-1 (63°45.42' S, 60°26.51' W; 633 m water depth) east of Trinity Island, PS97/068-2 (63°10.05' S, 59°18.12' W; 794 m water depth) in the Orleans Trough and PS97/072-2 (62°00.39' S, 56°03.88' W; 1992 m water depth) in the east Bransfield Basin (Fig. 1b). Smear slides were examined and microscopic description of the surface sediments was done onboard (Lamy, 2016). Immediately after recovery, sediment cores were sectioned into 1 cm slices and subsampled onboard. Samples designated for biomarker analyses were stored in glass vials at  $-20^{\circ}\text{C}$ , and samples for micropaleontological analyses were stored in plastic bags at  $+4^{\circ}\text{C}$ . A second suite of samples from a trigger core from

station PS97/072-1 was used for diatom analyses (diatom samples from core PS97/072-2 were not available).

Geochronology for the sediment cores from sites PS97/056-1 and PS97/072-2 was established using  $^{210}\text{Pb}_{\text{xs}}$  activities quantified by alpha spectrometry of its daughter  $^{210}\text{Po}$  in secular equilibrium with  $^{210}\text{Pb}$  and using  $^{209}\text{Po}$  as a yield tracer (Flynn, 1968). The activities were corrected to the time of plating considering the  $^{210}\text{Po}$  decay (half-life: 138 d).  $^{210}\text{Pb}_{\text{xs}}$  (unsupported) activities were determined as the difference between  $^{210}\text{Pb}$  and  $^{226}\text{Ra}$  activities measured by gamma spectrometry in some intervals of the sediment core. Alpha and gamma counting was performed at the Laboratoire Géosciences of the Université de Montpellier (France). The ages were based on  $^{210}\text{Pb}_{\text{xs}}$  inventories according the constant rate of supply model (CRS; Appleby and Oldfield, 1978). Standard deviations (SDs) were estimated, propagating the counting uncertainties (Bevington et al., 1993). Since the dating of cores PS97/056-1 and PS97/072-2 was done on selected samples the age model was established using the software R (R Core Team, 2012) and the package clam (Blaauw, 2010; version 2.3.2, calibration curve Marine13.14C). Trigger core PS97/072-1 was correlated with the age model of core PS97/072-2 based on TOC data (see Fig. S1 in the Supplement).

$^{210}\text{Pb}_{\text{xs}}$  for core PS97/068-2 was measured at the Alfred Wegener Institute (AWI, Germany) on dried and ground bulk sediment samples in sealed gas-tight petri dishes using an HPGe gamma spectrometer with planar geometry.  $^{210}\text{Pb}$  was measured at 46 keV, and  $^{226}\text{Ra}$  was measured for the excess correction in each depth interval via its indirect decay products at 295, 352 and 609 keV. Analytical errors were calculated with consideration of error propagation. For core PS97/068-2 the calculation of CRS ages and the Monte Carlo approximation of age uncertainties were based on Sanchez-Cabeza et al. (2014), modified to accommodate the variable sample sizes and fractions for different depths. Due to residual inventory of  $^{210}\text{Pb}_{\text{xs}}$  below the available samples in cores PS97/056-1 and PS97/072-2, the CRS model had increasing uncertainties below  $\sim 130$  years (Fig. S2). We therefore extrapolated ages before 1880 based on the average respective sedimentation rates for the oldest 3 cm (Fig. 2).

## 2.3 Organic geochemical analyses

Organic geochemical analyses were done on freeze-dried and homogenized sediments. Bulk contents of carbon (C) and nitrogen (N) were determined on 30 mg sediment samples with a CNS analyzer (Elementar Vario EL III, standard error  $< 2\%$ ), whereas the analysis of TOC content was done on a 0.1 g acidified (500  $\mu\text{L}$  hydrochloric acid) sediment sample using a carbon–sulfur determinator (CS-2000, ELTRA, standard error  $< 0.6\%$ ). The C/N ratio was calculated as TOC/total nitrogen.

The extraction procedure of HBIs follows the analytical protocol of the international community for conducting HBI-

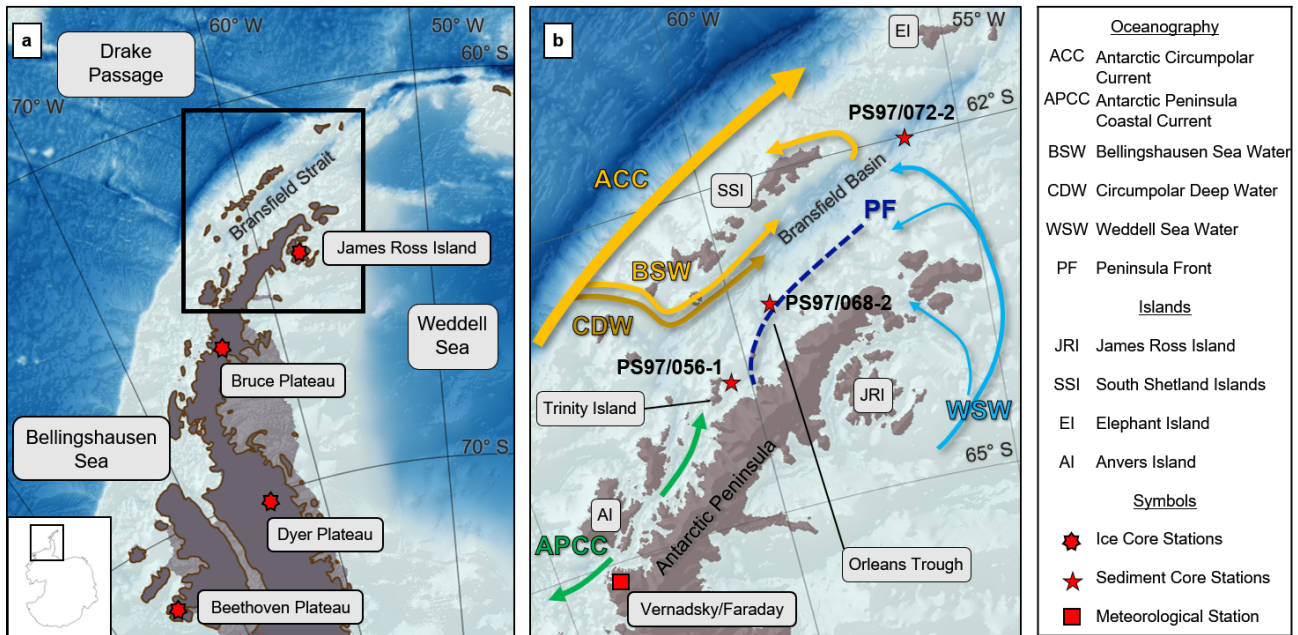


**Figure 1.** (a) Overview map of the Antarctic Peninsula with the position of the ice cores from Dyer Plateau, Beethoven Plateau, James Ross Island (Abram et al., 2010) and Bruce Plateau (Goodwin et al., 2016) as well as bathymetric features in the Bellingshausen Sea, the Weddell Sea and the Drake Passage. (b) Oceanographic setting in the study area (modified after Hofmann et al., 1996; Moffat and Meredith, 2018; Sangrà et al., 2011), sediment and ice core sites, and geographic locations mentioned in the text. Maps were generated with QGIS 3.0 (2018), and the bathymetry was taken from GEBCO\_14 from 2015.

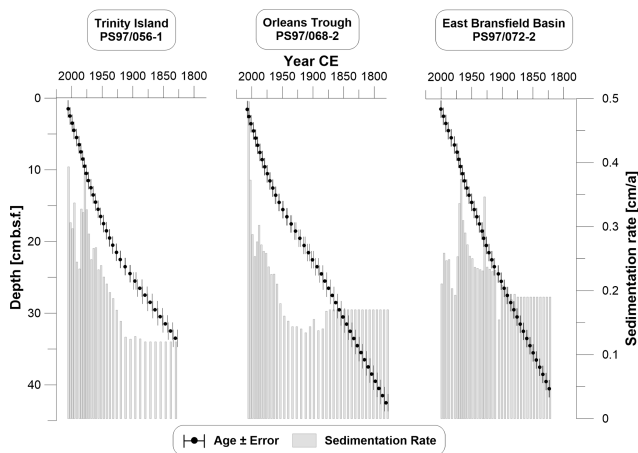


**Figure 2.** Age–depth models with error bars for all three cores. The sedimentation rate is displayed as grey bars. Ages are based on radiometric dating and were extrapolated prior to 1880 CE for all cores based on the average respective sedimentation rate of the three lowermost reliably dated intervals. All plots were done with Grapher™ 13.

based sea ice reconstructions (Belt et al., 2013, 2014; Stein et al., 2012). For the quantification of biomarkers the internal standards 7-hexylnonadecane (7-HND; HBI standard),  $5\alpha$ -androstan- $3\beta$ -ol (sterol standard) and  $C_{46}$  (GDGT standard) were added to the sediments. Sediment samples of

5 g were processed ultrasonically three times using 6 mL of  $CH_2Cl_2$  : MeOH (v/v 2:1, 15 min), followed by centrifugation (2500 rpm, 1 min) and decantation of the total organic solvent extract. The different biomarkers were separated via open-column chromatography with silica gel used as a stationary phase. First, the apolar fraction containing HBIs was separated with 5 mL hexane, while the second polar fraction containing GDGTs and sterols was eluted with 5 mL of  $CH_2Cl_2$  : MeOH (v/v 1:1). The polar fraction (GDGT and sterols) was dried using nitrogen, redissolved in 120  $\mu$ L hexane:isopropanol (v/v 99:1) and filtered through a polytetrafluoroethylene filter (0.45  $\mu$ m in diameter). After measuring GDGTs, the polar fraction of the sample was silylated (200  $\mu$ L BSTFA; 60  $^{\circ}$ C; 2 h) and used for sterol analysis.

The HBIs and sterols were analyzed by GC-MS with an Agilent 7890B gas chromatograph equipped with a 30 m DB 1 MS column (0.25 mm diameter, 0.250  $\mu$ m film thickness) coupled to an Agilent 5977B mass spectrometer (MSD, 70 eV constant ionization potential, ion source temperature 230  $^{\circ}$ C). Apolar and polar lipid fractions were analyzed using different temperature programs. For HBIs, the temperature was held at 60  $^{\circ}$ C for 3 min, gradually increased to 325  $^{\circ}$ C over the course of 23 min, and sustained at this level for 16 min. Sterol analysis started at a temperature of 60  $^{\circ}$ C for 2 min; the temperature then gradually increased to 150  $^{\circ}$ C over the course of 6 min and continued to increase to 325  $^{\circ}$ C over a course 57 min. HBIs were identified via comparison

of mass spectra of the measured compounds and published mass spectra (Belt et al., 2000). Quantification of HBIs was based on manual peak integration. Instrumental response factors of molecular ions of HBI dienes ( $m/z$  348) and trienes ( $m/z$  346) were determined by means of calibration measurements using a sample with known concentrations of HBIs. Identification of sterols was based on comparison of their retention times and mass spectra with those of reference compounds analyzed with the same instrument. The mean relative error of duplicates was  $< 5\%$  for HBIs and  $< 1\%$  for sterols (desmosterol had exceptionally high relative errors of up to  $14\%$ ), and the detection limit was determined at  $0.5$  ng per gram of sediment. Co-elution of other compounds hampered identification and quantification of sterols in several samples (PS97/056-1; 0–13 cm and PS97/072-2; 0–16 cm). Concentrations of HBIs and sterols were normalized to TOC contents ( $\mu\text{g}$  per gram of TOC).

GDGTs were analyzed using high-performance liquid chromatography (HPLC; Agilent 1200 series HPLC system) coupled to a single quadrupole mass spectrometer (MS; Agilent 6120 MSD) via an atmospheric pressure chemical ionization (APCI) interface. Individual GDGTs were separated at  $30^\circ\text{C}$  on a Prevail Cyano column ( $150\text{ mm} \times 2.1\text{ mm}$ ,  $3\ \mu\text{m}$ ). Each sample was injected ( $20\ \mu\text{L}$ ) and passed a 5 min isocratic elution with mobile phase A (hexane–2-propanol–chloroform; 98 : 1 : 1) at a flow rate of  $0.2\text{ mL min}^{-1}$ . The mobile phase B (hexane–2-propanol–chloroform; 89:10:1) increased linearly to  $10\%$  within 20 min and after this to  $100\%$  within 10 min. After 7 min the column was cleaned with a backflush (5 min, flow  $0.6\text{ mL min}^{-1}$ ) and re-equilibrated with solvent A (10 min, flow  $0.2\text{ mL min}^{-1}$ ). The APCI had the following conditions: nebulizer pressure 50 psi, vaporizer temperature  $350^\circ\text{C}$ ,  $\text{N}_2$  drying gas temperature  $350^\circ\text{C}$ , flow  $5\text{ L min}^{-1}$ , capillary voltage 4 kV and corona current  $5\ \mu\text{A}$ . GDGT detection was done by selective ion monitoring (SIM) of  $(\text{M}+\text{H})^+$  ions (dwell time 76 ms). The molecular ions  $m/z$  of GDGT-I ( $m/z$  1300), GDGT-II ( $m/z$  1298), GDGT-III ( $m/z$  1296) and crenarchaeol ( $m/z$  1292) as well as of the branched GDGT-Ia ( $m/z$  1022), GDGT-IIa ( $m/z$  1036), GDGT-IIIa ( $m/z$  1050) and hydroxylated GDGTs OH-GDGT-0 ( $m/z$  1318), OH-GDGT-1 ( $m/z$  1316) and OH-GDGT-2 ( $m/z$  1314) were quantified in relation to the internal standard  $\text{C}_{46}$  ( $m/z$  744). The hydroxylated GDGTs were quantified in the scans of their related GDGTs (see Fietz et al., 2013). The standard deviation was 0.01 units of  $\text{TEX}_{86}^{\text{L}}$ .

We follow the recommendation of Fietz et al. (2020) and apply both hydroxylated and non-hydroxylated GDGT temperature estimations because their significance for different ocean regions is still the subject of many discussions (Fietz et al., 2016; Hugué et al., 2013; Liu et al., 2012; Lü et al., 2015; Schouten et al., 2013), especially for low-temperature paleo-events at continental margins (Wang et al., 2015). After Kalanetra et al. (2009) GDGT-derived temperatures represent near-surface waters, which is underlined by studies from

Kim et al. (2012) and Park et al. (2019), and we therefore consider our results to reflect subsurface ocean temperatures (SOTs). For calculation of  $\text{TEX}_{86}^{\text{L}}$  (Kim et al., 2010) only GDGTs with the  $m/z$  1296 (GDGT-3),  $m/z$  1298 (GDGT-2) and  $m/z$  1300 (GDGT-1) were considered in Eq. (1),

$$\text{TEX}_{86}^{\text{L}} = \log \left( \frac{[\text{GDGT} - 2]}{[\text{GDGT} - 1] + [\text{GDGT} - 2] + [\text{GDGT} - 3]} \right), \quad (1)$$

and calibrated it with Eq. (2):

$$\text{SOT}^{\text{TEX}} = 67.5 \times \text{TEX}_{86}^{\text{L}} + 46.9 \quad (2)$$

(Kim et al., 2010).

The calculation based on OH-GDGT was done after Lü et al. (2015) in Eq. (3),

$$\text{RI} - \text{OH}' = \frac{[\text{OH} - \text{GDGT} - 1] + 2 \times [\text{OH} - \text{GDGT} - 2]}{[\text{OH} - \text{GDGT} - 0] + [\text{OH} - \text{GDGT} - 1] + [\text{OH} - \text{GDGT} - 2]}, \quad (3)$$

and calibrated with Eq. (4):

$$\text{SOT}^{\text{OH}} = (\text{RI} - \text{OH}' - 0.1) / 0.0382. \quad (4)$$

We assume that both  $\text{SOT}^{\text{TEX}}$  and  $\text{SOT}^{\text{OH}}$  reflect annual mean temperatures because their calibrations are based on annual mean SST (Kim et al., 2010; Lü et al., 2015).

To determine the influence of terrestrial organic matter the branched and isoprenoid tetraether (BIT) index was calculated following Hopmans et al. (2004) as Eq. (5).

$$\text{BIT} = \frac{[\text{GDGT} - \text{Ia}] + [\text{GDGT} - \text{IIa}] + [\text{GDGT} - \text{IIIa}]}{[\text{crenarchaeol}] + [\text{GDGT} - \text{Ia}] + [\text{GDGT} - \text{IIa}] + [\text{GDGT} - \text{IIIa}]} \quad (5)$$

The phytoplankton IPSO<sub>25</sub> index (PIPSO<sub>25</sub>) was calculated following Eq. (6) from Vorrath et al. (2019) with

$$\text{PIPSO}_{25} = \frac{\text{IPSO}_{25}}{\text{IPSO}_{25} + (c \times \text{phytoplankton marker})} \quad (6)$$

using sterols and HBI trienes as phytoplankton markers (Vorrath et al., 2019). The balance factor  $c$  ( $c = \text{mean IPSO}_{25} / \text{mean phytoplankton biomarker}$ ) is used to account for concentration offsets between IPSO<sub>25</sub> and phytoplankton biomarkers (Belt and Müller, 2013; Müller et al., 2011; Smik et al., 2016b; Vorrath et al., 2019). Since the concentrations of HBI trienes are within the same range as the sea ice proxy, we set the  $c$  factor to 1 (Smik et al., 2016b) and  $c$  factors for sterols were calculated individually for every core site. To distinguish the different indices based on their phytoplankton marker we use the terms  $\text{P}_Z\text{IPSO}_{25}$  for an index based on Z-trienes,  $\text{P}_E\text{IPSO}_{25}$  based on E-trienes,  $\text{P}_B\text{IPSO}_{25}$  based on brassicasterol and  $\text{P}_D\text{IPSO}_{25}$  based on dinosterol.

## 2.4 Diatom analysis and transfer functions

Diatom analyses were done on 94 samples in total. Every second centimeter of core PS97/056-1 and every centimeter

of core PS97/068-2 and trigger core PS97/072-1 was analyzed. About 300 mg of freeze-dried sediments was treated after the method described by Cárdenas et al. (2019), and slides for microscopy analysis were prepared after Gersonde and Zielinski (2000). Two permanent slides per sample were prepared and observed with a Carl Zeiss Axio Lab.1 microscope with phase contrast at 1000 $\times$  magnification at the Instituto Antártico Chileno in Punta Arenas. Diatoms were identified and counted on transects on microslides until reaching at least 400 valves on each slide, following counting procedures of Schrader and Gersonde (1978). Diatom identification was done to species or species group level following the taxonomy described by Armand and Zielinski (2001), Taylor et al. (2001), Crosta et al. (2004), Buffen et al. (2007), Cefarelli et al. (2010), Esper et al. (2010), Allen (2014) and Campagne et al. (2016). The *Hyalochaete* of the genus *Chaetoceros* were identified as vegetative cells and/or resting spores.

We applied the marine diatom transfer function TF MAT-D274/28/4an to estimate WSI concentrations. It comprises 274 reference samples, including two samples from the AP, with 28 diatom taxa and/or taxonomic groups and an average of four analogues from surface sediments that cover the complete circumpolar Antarctic in the Atlantic, Pacific and western Indian sectors of the Southern Ocean (Esper and Gersonde, 2014a). WSI estimates reflect September sea ice concentrations averaged over the period 1981–2010 (National Oceanic and Atmospheric Administrations, NOAA; Reynolds et al., 2002, 2007) in a 1  $\times$  1 grid. We follow the approach of Zwally et al. (2002) and define a sea ice concentration of 15 % as the threshold for the presence or absence of sea ice and 40 % as the representative average of the sea ice edge (Gersonde et al., 2005; Gloersen et al., 1993). For SSST, we used the transfer function TF IKM336/29/3q from 336 reference samples (covering all sectors of the Pacific, Atlantic and Indian Southern Ocean; four samples from the AP) with 29 diatom taxa and three factors (Esper and Gersonde, 2014b). For calculations of MAT and IKM the software R (R Core Team, 2012) was used with the packages *vegan* (Oksanen et al., 2012) and *analogue* (Simpson and Oksanen, 2012).

## 2.5 Modeled data

We used data from numerical modeling to compare and evaluate our biogeochemical proxies. The AWI-ESM2 is a state-of-the-art coupled climate model developed by Sidorenko et al. (2019). The model consists of the atmospheric model ECHAM6 (Stevens et al., 2013) and a finite-element sea ice–ocean model (FESOM2) (Danilov et al., 2017). It also includes a land surface model (JSBACH) with static ice sheets and dynamical vegetation (Raddatz et al., 2007).

The atmosphere grid in the high-resolution experiment is T63 (about 1.9 $^\circ$  or 210 km) with 47 vertical levels. A multi-resolution approach is employed in the ocean module. In detail, the high-resolution experiment applies up to 20 km hor-

izontal resolution over the Arctic and Antarctic region and 150 km for the far-field ocean (Fig. S3). Moreover, the tropical belt has a refined resolution of 30–50 km in this configuration. We used a fixed ice sheet and the topography was taken from ICE6G (Peltier et al., 2015), so isostatic adjustments are neglected. There are 46 uneven vertical depths in the ocean component. The model has been validated under modern climate conditions (Sidorenko et al., 2019). Previous versions of the model have been applied for the Holocene (Shi et al., 2020; Shi and Lohmann, 2016).

We ran the climate model from the mid-Holocene as a starting point (*midHolocene* simulation) and performed a transient simulation from the mid-Holocene to the preindustrial (*past6k* simulation) as described in Otto-Bliesner et al. (2017). The transient orbital parameters are calculated according to Berger (1978). Moreover, as the change in topography from the mid-Holocene to the present is minor, we use constant topography under preindustrial conditions for the entire transient period. In our modeling strategy, we follow Lorenz and Lohmann (2004) and use the climate condition from the preindustrial state as spin-up and initial state for the transient simulation covering the period 1850–2017 CE. Greenhouse gases concentrations are taken from ice core records (Köhler et al., 2017) and from Meinshausen et al. (2011).

## 2.6 Additional data sets

Regional monthly satellite sea ice concentrations were derived from Nimbus-7 SMMR and DMSP SSM/I-SSMIS passive microwave data from the National Snow and Ice Data Center (NSIDC, grid cell size 25  $\times$  25 km; Cavalieri et al., 1996), and mean winter (JJA) and spring (SON) sea ice concentrations were used in this study.

For the large-scale atmospheric modes we used the paleo-ENSO index from Li et al. (2013), which covers the past 200 years, and the modeled SAM data from Abram et al. (2014).

We used ice core stable isotope data representing relative air temperature at James Ross Island ( $\delta$ D; Abram et al., 2013) and at Bruce Plateau ( $\delta^{18}$ O; Goodwin et al., 2016). We compared the marine sea ice proxies (biomarkers, diatoms) with MSA data from the West Antarctic Dyer Plateau ice core (Abram et al., 2010) and annual net snow accumulation from Bruce Plateau ( $A_n$ ; Goodwin et al., 2016).

## 3 Results

### 3.1 Age model and core description

The  $^{210}$ Pb signals indicated continuously increasing ages with depth in all sediment cores (Fig. 2). All sediment cores roughly cover the last 240 years (including the extrapolated time) with a resolution between 2 and 12 years per centimeter and sedimentation rates from 0.1 to 0.5 cm a $^{-1}$ . Core PS97/056-1 located east of Trinity Island is characterized by

silt-bearing diatomaceous clay (Lamy, 2016) and covers the time span from 1830 to 2006 CE with sedimentation rates increasing from 0.1 to 0.4  $\text{cm a}^{-1}$  over time. Core PS97/068-2 from Orleans Trough mainly consists of diatom-bearing silty clay (Lamy, 2016) and spans from 1780 to 2007 CE with sedimentation rates from 0.1 to 0.5  $\text{cm a}^{-1}$ . Sediment core PS97/072-2 from the east Bransfield Basin is the record from the greatest depth and characterized as silt-bearing diatomaceous clay (Lamy, 2016) with increasing sedimentation rates (from 0.1 to 0.4  $\text{cm a}^{-1}$ ) covering the time from 1823 to 2000 CE. At all three core sites, sedimentation rates increase towards the present. The TOC contents of all cores ranged between 0.7 and 1.1 wt %, with higher contents in younger sediments. Low C/N ratios ( $< 8.6$ ) and BIT values ( $< 0.02$ ) point to a marine origin of the organic matter.

### 3.2 Biomarker lipids

A summary of biomarker results is visualized in Fig. 3 (results of HBI E-trienes, sterols and their related sea ice indices can be found in Fig. S4). IPSO<sub>25</sub> is abundant at all core sites with values ranging from 0.2  $\mu\text{g g}^{-1}$  TOC up to 6.4  $\mu\text{g g}^{-1}$  TOC. All three cores display similar patterns, with low IPSO<sub>25</sub> concentrations before 1850 CE, followed by moderate concentrations until 1970 CE and maxima in the 2000s (Fig. 3). Concentrations of HBI trienes are much lower than IPSO<sub>25</sub> concentrations, with values below 1.4  $\mu\text{g g}^{-1}$  TOC for Z-trienes (Fig. 3) and below 0.7  $\mu\text{g g}^{-1}$  TOC for E-trienes (Fig. S4). The exception is core PS97/072-2 from the east Bransfield Basin where both HBI trienes reach up to 3.7  $\mu\text{g g}^{-1}$  TOC and 1.6  $\mu\text{g g}^{-1}$  TOC, respectively, in the second half of the 19th century. The concentrations of brassicasterol (10.2–241.3  $\mu\text{g g}^{-1}$  TOC) and dinosterol (5.0–145.2  $\mu\text{g g}^{-1}$  TOC) are 2 to 3 orders of magnitude higher than those of the HBIs; markedly lower concentrations characterize the Orleans Trough (PS97/068-2) (Fig. S4). The PIPSO<sub>25</sub> indices calculated with Z- and E-trienes run parallel to PIPSO<sub>25</sub> based on brassicasterol and dinosterol and show increasing trends with time. In general, the HBI triene-based PIPSO<sub>25</sub> indices have higher values ( $P_Z$ IPSO<sub>25</sub> from 0.32 to 0.91;  $P_E$ IPSO<sub>25</sub> from 0.25 to 0.95) than the PIPSO<sub>25</sub> indices based on sterols ( $P_B$ IPSO<sub>25</sub> from 0.15 to 0.70;  $P_D$ IPSO<sub>25</sub> from 0.11 to 0.75). The PIPSO<sub>25</sub> indices suggest an increasing spring sea ice cover over time (Figs. 3 and S4). This is most prominent at the east Bransfield Basin (PS97/072-2) where the lowest sea ice cover is indicated around 1870 CE, and an increase towards the present is indicated. Indications of short-term low spring sea ice cover are found for the 1960s and 1970s at the near-coastal core sites (PS97/056-1 and PS97/068-2) but do not change the overall trend. A clear stratigraphy is hard to distinguish, so we focus on units that reflect similar sea ice conditions taken from our sea ice proxies (Fig. 3). We clearly stress out that our age models were extrapolated before 1880, and hence the age uncertainty increases in this period.

Temperatures based on GDGTs show a wide range of values. At Trinity Island (PS97/056-1) and the east Bransfield Basin (PS97/072-2), SOT<sup>TEX</sup> ranges from  $-3.89$  to  $2.3$  °C (Fig. 3), whereas temperatures are always above zero from 0.7 to 3.6 °C at the Orleans Trough (PS97/068-2). Distinct cold events occur in the 1860s in the east Bransfield Basin (PS97/072-2) and as a longer cool period from 1940 to 1970 CE at the coastal core sites, but general trends are hard to distinguish. In contrast, SOT<sup>OH</sup> displays a decreasing temperature trend at all core sites with a narrow range of  $-2.56$  to  $-1.0$  °C reversed by a rapid warming since the 1990s (Fig. 3). As some temperatures lie below the freezing point of seawater we assume that neither SOT<sup>TEX</sup> nor SOT<sup>OH</sup> may reflect exact temperatures but temperature trends at each core site.

### 3.3 Diatom assemblages

WSI estimations derived from diatom assemblages point to a high variability (74 % to 92 % WSI at PS97/056-1, 64 % to 92 % at PS97/068-2, 68 % to 90 % at PS97/072-1), with minimum sea ice concentrations around 1840 and 1880 CE and a slight increment toward 1990s (Fig. 3). This variability coincides with abundances of the sea ice diatom species *Fragilariopsis curta* that shows higher values in cores PS97/056-1 (abundance range 0.1 %–1.8 %) and 068-2 (abundance range 2.0 %–10.7 %) in the second half of the 20th century (Fig. 3), while no trends are present in PS97/072-1 (abundance range 1.9 %–7.6 %). In addition, WSI records reveal similar features compared to IPSO<sub>25</sub> and PIPSO<sub>25</sub>, which points to an expected coherence of winter and spring sea ice estimates based on different proxies. The SSSTs from diatom assemblages have a small amplitude in all cores ( $-0.9$  to  $0.5$  °C at PS97/056-1,  $-1.1$  to  $0.2$  °C at 068-2 and  $-0.8$  to  $0.1$  °C at 072-1) and show a similar pattern as SOT<sup>TEX</sup> at the sites PS97/068-2 and 072-1 (Fig. 3).

### 3.4 Modeled data

We use model data as derived from the AWI-ESM2, which includes spring sea ice concentration (mSSIC), spring sea ice thickness (mSSIT), subsurface ocean temperature (mSOT, mean temperature from 30–100 m below the sea surface) and surface air temperature (mSAT). Based on 10-year means, we detect negative trends for the last 200 years in both mSSIC (decrease by 30 % to 50 %) and mSSIT (decrease from 0.5 m down to 0.1 m). At the same time, positive trends for mSOT and mSAT at all core sites show temperatures rising by 0.3 to 0.6 °C. Further, a time series of the latitudinal shift of the sea ice edge at the WAP (between 50 and 70° W) shows a southward shift of 1.5° from 61.9 to 63.4° S in the 20th century.

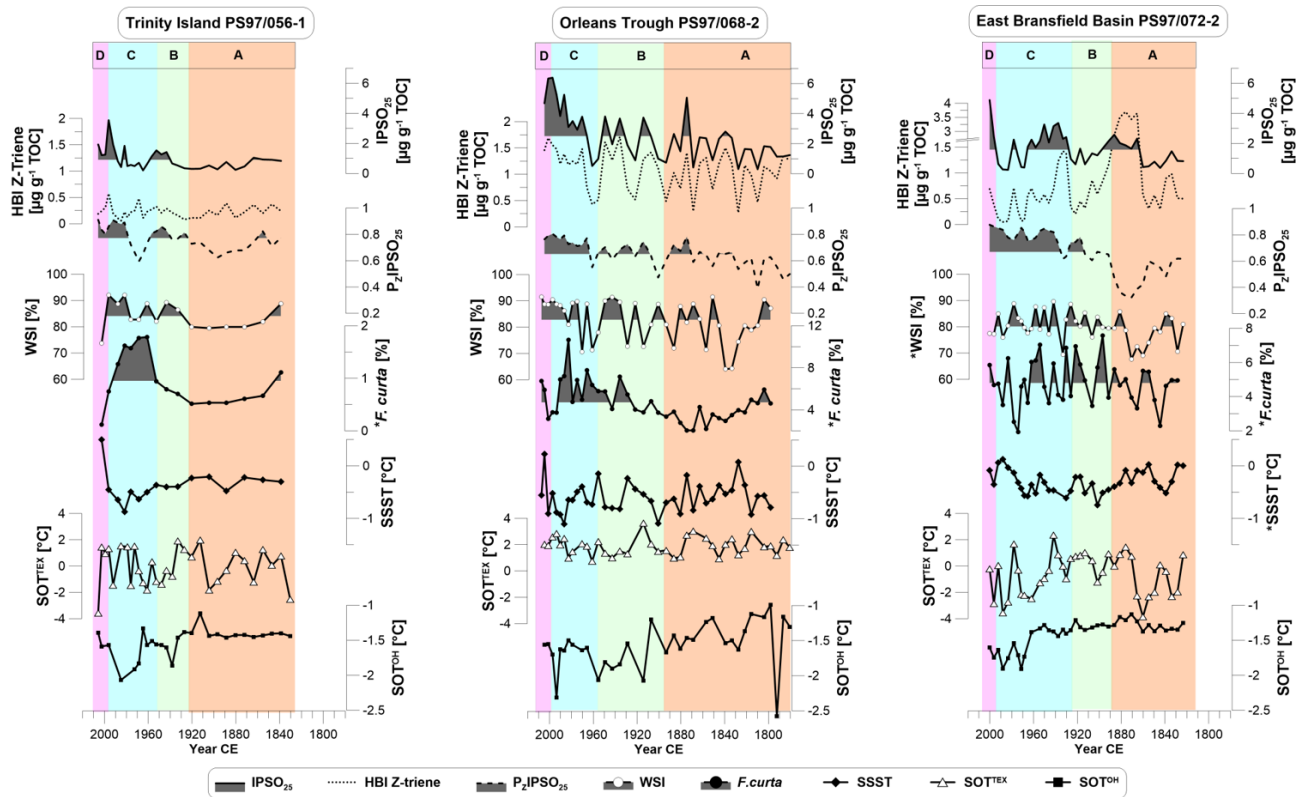


**Figure 3.** Biomarker composition of the three sediment cores showing concentrations of (from top to bottom) IPSO<sub>25</sub> and HBI Z-trienes, the sea ice index P<sub>2</sub>IPSO<sub>25</sub>, diatom-derived winter sea ice (WSI) concentrations, abundance of *F. curta*, summer sea surface temperatures (SSSTs), subsurface ocean temperature derived from TEX<sub>86</sub><sup>L</sup> (SOT<sup>TEX</sup>), and OH-GDGTs (SOT<sup>OH</sup>). Data marked with \* are from the trigger core PS97/072-1. Vertical colored bars denote the environmental units A to D described in Sect. 4.5. The shading marks values above the mean of each biomarker in the respective core.

## 4 Discussion

### 4.1 Spatial and temporal distribution of paleoenvironmental biomarkers

The core site at Trinity Island (PS97/056-1) is dominated by the APCC and receives freshwater input from the peninsula, with an influence of BSW from the ACC (Moffat and Meredith, 2018). We suggest that sea ice proxies originate from free-floating or landfast sea ice and are impacted by meltwater discharge in this region since the core site is only 8 km away from Trinity Island. Coastal upwelling of macronutrients and micronutrients, especially iron, and a stratified water column fuel open marine primary production (Sanchez et al., 2019; Vernet et al., 2008) and may explain the highest concentrations of sterols at this core site. IPSO<sub>25</sub>, HBI Z-triene, P<sub>2</sub>IPSO<sub>25</sub>, WSI and *F. curta* records exhibit similar trends and fluctuations over time (Fig. 3), but a direct relation between reconstructed sea ice conditions and temperature (SSST, SOT<sup>TEX</sup> and SOT<sup>OH</sup>) is not evident. However, slightly higher temperatures deduced from SOT<sup>OH</sup> and diatom SSST seem to coincide with lower IPSO<sub>25</sub> concentrations, lower PIPSO<sub>25</sub> values, and reduced WSI and *F. curta*

content in the 19th century, while variable but higher temperatures in the 20th century are accompanied by higher IPSO<sub>25</sub> and WSI concentrations at site PS97/056-1 (Fig. 3). The remarkably low SOT<sup>TEX</sup> in the year 2006 CE might be a result of cold meltwater injections due to enhanced glacier melting (e.g., Pastra Glacier on Trinity Island). At the same time, high SSST and SOT<sup>OH</sup> as well as a low WSI point towards a significantly warm period around the year 2006, which is underlined by meteorological station data (Turner et al., 2019). A weak cooling trend is present in SSST and SOT<sup>OH</sup> from 1920 CE to the 1990s, followed by a warming towards the present.

Given the position of the sediment core PS97/068-2 in the Orleans Trough, we suggest that the core site is affected by the Peninsula Front where water masses from both salty and cold WSW and fresh and warm BSW meet. The water column here is characterized by enhanced mixing within a narrow eddy zone and deepening of the mixed layer (Sangrà et al., 2011). High concentrations of biomarkers indicate a strengthening of primary productivity associated with BSW (Gonçalves-Araujo et al., 2015) in a less stratified and mixed water column (Vernet et al., 2008). The patterns of IPSO<sub>25</sub>,

HBI Z-triene, P<sub>Z</sub>IPSO<sub>25</sub>, WSI and *F. curta* have a good visual correspondence. They indicate higher phytoplankton productivity and higher sea ice cover towards the present time. The SOT<sup>TEX</sup> is remarkably high (above 0 °C) throughout the studied period, contrasting with modern ocean temperatures that are below −0.5° in the upper 400 m along the WAP (Cook et al., 2016). Assuming that enhanced mixing of water masses with the atmosphere leads to warmer ocean temperatures, this must be evident in our other temperature records. However, since none of the other temperature proxies show such a response we must treat this record with caution. We note that OH-based records seem to better reflect temperature estimations in polar regions (Fietz et al., 2020) and suppose that water mixing might have a disturbing effect of TEX-based temperature reconstructions. Compared to SOT<sup>TEX</sup>, SOT<sup>OH</sup> temperatures are closer to modern ocean temperatures in this area (−0.5 °C; Cook et al., 2016) within a narrow range. Since this core site is located at the Peninsula Front (i.e., in the middle of BSW and WSW), no clear dominance of one water mass or the other is evident. Ocean temperatures below 0 °C indicate the influence of WSW, while high biomarker concentrations refer to higher primary production as is suggested for the BWS (Gonçalves-Araujo et al., 2015).

The core site in the east Bransfield Basin (PS97/072-2) is further away from the coast (145 km) compared to the other two core sites. Marine productivity is expected to be lower due to the presence of WSW (Gonçalves-Araujo et al., 2015), but relatively high concentrations of IP<sub>SO</sub><sub>25</sub> and HBI Z-triene may be related to fertilization through iron input from shelf waters (Frants et al., 2013). A remarkable maximum in HBI Z-triene concentrations in the late 19th century suggests drastic changes in the local oceanographic settings and productivity patterns. As indicated by SOT<sup>TEX</sup>, this period is marked by a rapid shift from cold to warm subsurface ocean temperatures, pointing to a possible dominance of warmer BSW. A corresponding retreat of sea ice cover and likely ice-free summers, as reflected by P<sub>Z</sub>IPSO<sub>25</sub> and WSI values, could have promoted the productivity of open marine or coastal phytoplankton communities, e.g., *Rhizosolenia* and *Pleurosigma*, synthesizing the HBI Z-triene (Belt et al., 2000, 2017). Sea ice proxies show less pronounced increasing trends at this core site compared to the near-coastal records. At all three core sites the sedimentation rates increase towards the present. Together with higher TOC contents we suggest this to be linked to a higher export of organic matter, although primary production tended to decrease in the past 30 years (Montes-Hugo et al., 2009).

We note that for the interpretation of biomarker-based sea ice reconstructions the potential degradation of biomarkers affecting their downcore concentration profile needs to be taken into consideration. We observe that the upper part of the sediment cores contains higher concentrations of IP<sub>SO</sub><sub>25</sub>, HBI trienes and sterols compared to the underlying older sediments. A similar pattern in IP<sub>SO</sub><sub>25</sub> and HBI triene con-

centrations is also reported by Barbara et al. (2013). Their biomarker concentrations from the southern WAP equal the concentrations in the Bransfield Strait, but high values near the sediment surface, as in our data, are not present. Auto- and photooxidative degradation of IP<sub>SO</sub><sub>25</sub> and HBI trienes was already studied in laboratory experiments (Rontani et al., 2014, 2011), and autooxidative and bacterial degradation was also found in the oxic layers of surface sediments (Rontani et al., 2019). According to these results, a faster degradation of HBI trienes (because of their higher number of double bonds) in the upper centimeters of the sediment cores studied herein would lead to higher PIPSO<sub>25</sub> values with progressive degradation. Sterols might also undergo degradation (Rontani et al., 2012), but studies from Antarctic sediments are still missing. However, as we observe remarkably high HBI triene concentrations in core PS97/072-2 in the late 20th century and lower concentrations towards the present (Figs. 3 and S4), we suggest that degradation may not have a major impact on biomarker concentrations presented in this study.

#### 4.2 Comparison of proxy-derived and modeled sea ice estimates with satellite sea ice observations

We compare IP<sub>SO</sub><sub>25</sub> concentrations, P<sub>Z</sub>IPSO<sub>25</sub> values, diatom-based WSI estimates and *F. curta* content with satellite data and with mSSIC to evaluate their accuracy in reflecting spring and winter sea ice cover variability at the core sites over the past 40 years (Fig. 4). Satellite-derived spring sea ice concentrations (satSSIC) show general similarities to fluctuations observed in the IP<sub>SO</sub><sub>25</sub> record, indicating lower sea ice cover in the 1980s, a peak in the mid-1990s, a drop in sea ice cover in the early 2000s and then a rise again in sea ice concentrations (Fig. 4).

At the near-coastal core sites (PS97/056-1 and 068-2), these dynamics are well reflected in IP<sub>SO</sub><sub>25</sub> and PIPSO<sub>25</sub>, in particular for site PS97/056-1, where a good correspondence is observed between biomarker and satellite data (Fig. 4). However, we cannot exclude aliasing effects due to a lower temporal resolution of the sediment cores (Pisias and Mix, 1988). Maximum sea ice concentrations observed in 1996 CE are well reflected by elevated IP<sub>SO</sub><sub>25</sub> concentrations, but the drop afterwards is not mirrored by biomarker data. Diatom-based WSI concentrations compared to satellite-derived winter sea ice concentrations (satWSIC) show that these two data sets are in moderate agreement at the near-coastal core sites (PS97/056-1 and PS97/068-2), and winter sea ice coverage seems to be less dynamic at the Peninsula Frontal mixing zone (PS97/068-2). It was already observed that WSI indicated much higher sea ice cover than satellite data (Vorrath et al., 2019) as the transfer function for WSI is built on a different satellite reference data set and rather represents sea ice probability than sea ice cover (Esper and Gersonde, 2014a). We also note that the modeled spring sea ice cover is mostly opposite to satellite data, in particular during the 1990s and 2000s. Such bias is found to be common in recent sea ice

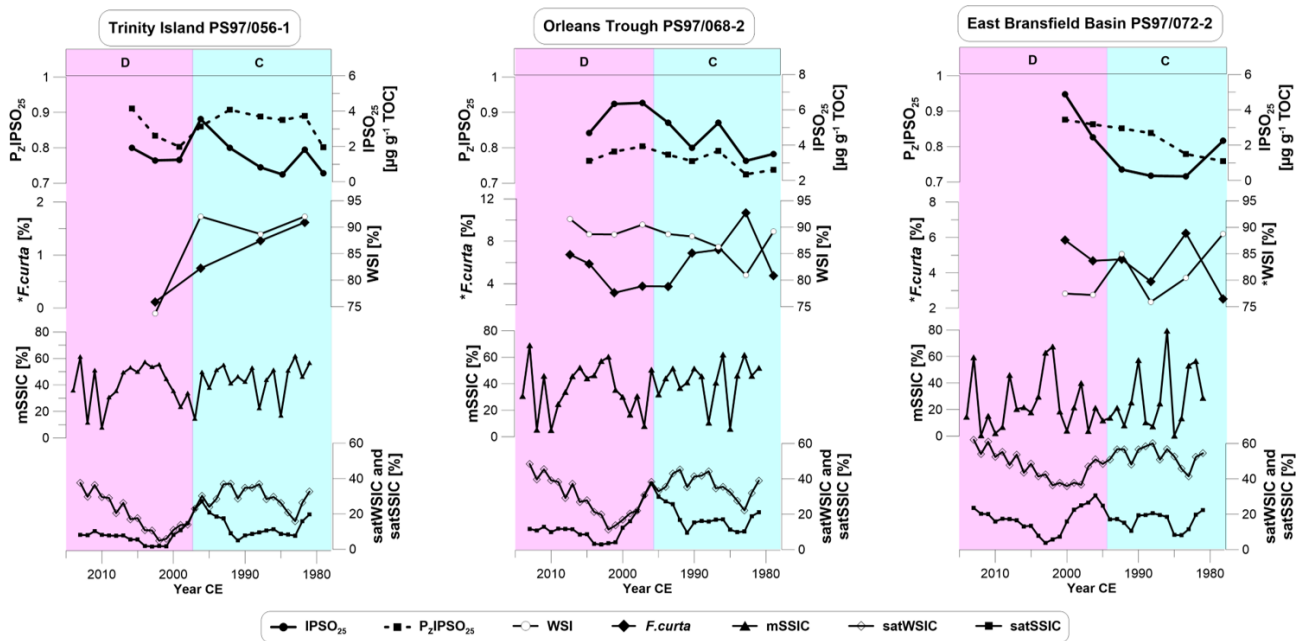


**Figure 4.** Concentrations of (from top to bottom) IPSO<sub>25</sub>, P<sub>z</sub>IPSO<sub>25</sub>, WSI and abundance of *F. curta* compared to modeled spring sea ice concentrations (mSSIC), and satellite-derived winter and spring sea ice concentrations (satWSIC and satSSIC, 5-year running mean) from the National Snow and Ice Data Center (NSIDC; Cavalieri et al., 1996) for all three core sites. Data marked with \* are from the trigger core PS97/072-1. Vertical bars denote the environmental units C and D.

modeling and can be traced back to the model's sensitivity to warming (Rosenblum and Eisenman, 2017) and the role of cloud feedbacks (Bodas-Salcedo et al., 2014). While modeled and satellite-derived data have similar ocean grid sizes (model: 30 × 30 km, satellite: 25 × 25 km), we suggest that global models such as AWI-ESM2 cannot resolve the AP sub-aerial and marine topography and have difficulties in capturing local to regional near-coastal sea ice dynamics in the study region. Another reason may relate to internal variability and missing feedbacks in the model, which makes a direct comparison of short time series difficult. Changes in the forcing are restricted to the insolation, and greenhouse gases and can affect the simulated climate by bringing in natural noises. For the 240 years of the modeled period, especially for small changes in the forcing, the internal variabilities can dominate the climate change, bringing difficulties to model–data comparisons. Feedbacks of aerosols, ozone, ice sheet dynamics, dust, and solar and volcano activity are missing because these elements were considered static in the model. Further, the modeled Antarctic sea ice is generally thicker and the coverage is higher due to a reduced warming of the Southern Ocean within the model setup (Sidorenko et al., 2019). However, both modeled and satellite data for all core sites show a decreasing trend in spring sea ice cover (about 10 %) and a slightly rising trend in winter sea ice cover over the 40-year period (about 7 %), while sea ice proxies suggest an increasing trend of spring sea ice. For winter sea ice, core sites PS97/056-1 and PS97/072-2 display a de-

creasing trend, whereas PS97/068-1 clearly points to an increase in winter sea ice.

For the offshore core site at the east Bransfield Basin (PS97/072-2), IPSO<sub>25</sub> and PIPSO<sub>25</sub> correspond better to satSSIC than to mSSIC sea ice data (Fig. 4). Between 1985 and 1995 CE, both PIPSO<sub>25</sub> indices suggest a similar increase in spring sea ice as in the satellite observations. Sea ice estimates from WSI and *F. curta* seem to better reflect satSSIC than satWSIC. Also, WSI estimates are remarkably lower than at the other core sites, although satellite winter sea ice cover is the highest of all.

Based on the overall accordance with satellite data, we conclude that the biomarker and diatom-based sea ice estimations are related to regional dynamics of sea ice cover, as far as we can assess it from the low resolution of the sediment cores. Regarding the oceanographic setting, we consider the fact that drift ice originating in the Weddell Sea may have also affected the deposition of IPSO<sub>25</sub>. Since HBI Z-trienes and sterol concentration profiles are similar to IPSO<sub>25</sub> concentrations (Figs. 3 and S4), we suggest that sea ice dynamics also promote growth of open marine phytoplankton species due to nutrient release or nutrient upwelling (Sanchez et al., 2019; Vernet et al., 2008). Input of allochthonous material from the shelf via near-bottom nepheloid layers is also possible (Palanques et al., 2002), which might impact the fidelity of the proxy records. As the record of satellite observations is short, it is not clear whether decadal or centennial sea ice trends can be directly derived from our biomarker records.

Also, the resolution of our sediment records is quite low (3 to 5 years) compared to satellite observations. Hence, we consider modeled and ice core data for further insights over the full sediment records.

#### 4.3 Comparison of sea ice proxy records with modeled and ice core data covering the pre-satellite era

By comparing IPSO<sub>25</sub>, P<sub>Z</sub>IPSO<sub>25</sub>-based sea ice estimates, WSI and *F. curta* with modeled spring sea ice data, we note opposite long-term sea ice trends reflected in the proxy records and the modeled data for the past 240 years (Fig. 5). Modeled spring sea ice concentration and thickness show clear decreasing trends at all sites, with a loss of sea ice cover between 15 % and 20 %. Modeled sea ice cover fluctuates strongly in the east Bransfield Basin (PS97/072-2), whereas the coastal core sites run almost parallel. Although the modeled spring sea ice does not agree with satellite data on the local to regional scale (Fig. 4), it does reflect the satellite observations regarding the large-scale general trend of sea ice decline and warming in the Bellingshausen Sea and at the WAP (Parkinson and Cavalieri, 2012; Vaughan et al., 2003) because the model is based on rising greenhouse gas concentrations in the 20th century.

The increasing concentrations of IPSO<sub>25</sub> and the rise of parallel-running P<sub>Z</sub>IPSO<sub>25</sub> values, diatom-derived WSI concentrations and rising *F. curta* content recorded in all three sediment cores suggest a long-term sea ice advance. On the other hand, the increase in the concentrations of the HBI Z-triene and sterols would indicate more open marine and/or stable ice edge conditions promoting phytoplankton productivity. We suggest that a thinning of the ice and a hence higher light penetration permitting photosynthesis at the ice–water interface (Hancke et al., 2018) could have triggered the productivity of IPSO<sub>25</sub> source diatoms, even if sea ice extent would have been lower. Thinner ice and accelerated melting during spring may have resulted in a largely ice-free sea surface during summer, promoting phytoplankton (biomarker) productivity. In addition, increased melting of sea ice could have contributed to higher primary production by releasing nutrients in a stabilized water column. This could have led to a higher deposition of sea ice diatoms and IPSO<sub>25</sub> by sinking of these phytoplankton blooms during spring and summer (Palanques et al., 2002). The declining mSSIC and mSSIT (Fig. S5) support the interpretation of sea ice thinning. Therefore, we suggest that increasing concentrations of both IPSO<sub>25</sub> and phytoplankton-derived biomarker lipids accordingly reflect more pronounced ice edge conditions and/or a distinct seasonality in spring and summer conditions along the WAP over the past 240 years.

As the distribution of IPSO<sub>25</sub> is sensitive to local oceanographic conditions (Smik et al., 2016a), biomarker-based sea ice studies require an interpretation that takes the specific environmental characteristics of the region into account. In this context, we generally expect influences of meltwater input

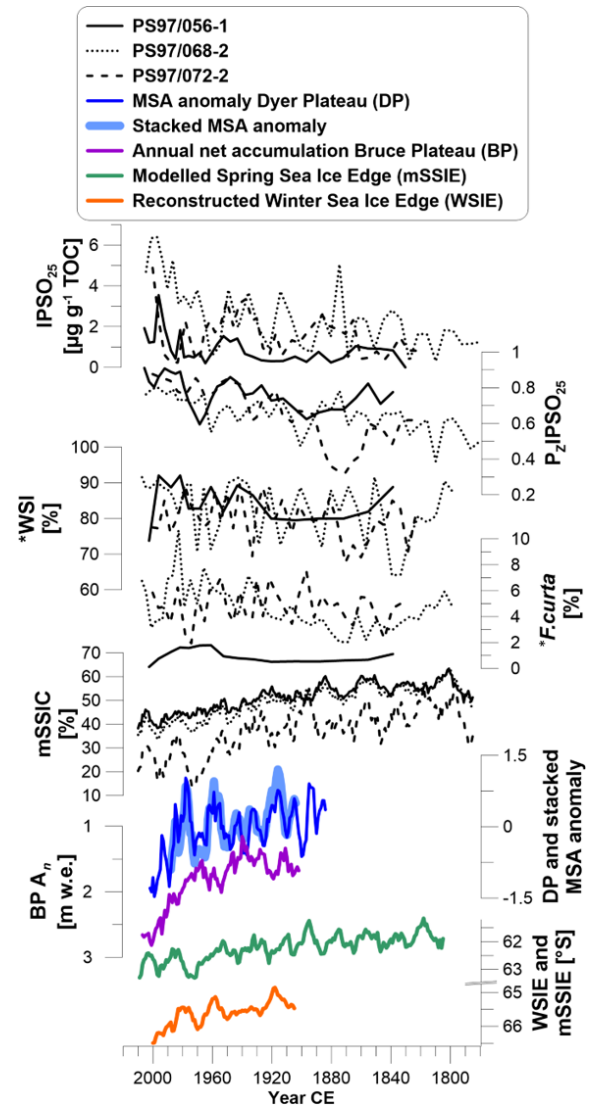


**Figure 5.** The biomarker (from top to bottom) IPSO<sub>25</sub>, sea ice index P<sub>Z</sub>IPSO<sub>25</sub>, winter sea ice concentration (WSI) from diatom assemblages and abundance of *F. curta* compared to modeled spring sea ice cover (mSSIC; 10-year running mean), MSA anomaly from Dyer Plateau, stacked MSA covering the Bellingshausen Sea sector (5-year running mean; Abram et al., 2010), annual net accumulation from Bruce Plateau (5-year running mean; Goodwin et al., 2016), modeled spring sea ice edge latitude (mSSIE; 10-year running mean) and reconstructed winter sea ice edge latitude from MSA (WSIE; 10-year running mean; Abram et al., 2010). Data marked with \* are from the trigger core PS97/072-1.

from glacial melting during summer (Meredith et al., 2018), additional nutrient input from the APCC and intense mixing at the Peninsula Front. We suggest that high fluctuations in sea ice cover, sea ice thickness and water temperature may stimulate phytoplankton growth rather than stable conditions with very high and long-lasting or low ice cover and/or an ice-free sea surface (e.g., Xiao et al., 2013). We hence strengthen the need to compare the individual concentration records of IPSO<sub>25</sub> and phytoplankton biomarkers rather than using the IPSO<sub>25</sub> (and PIPSO<sub>25</sub>) record alone to deduce sea ice conditions (see also Müller et al., 2011, 2012).

We further consider records of MSA, an organic aerosol archived within ice cores, which is associated with marine biological activity during sea ice breakup and which is used as a proxy for sea ice reconstructions. Influenced by timing, duration and spatial extent of sea ice breakup, MSA concentrations are linked to winter sea ice extent in some regions and summer productivity within the sea ice zone in other regions of Antarctica (Thomas et al., 2019, and references therein). Here we use records of MSA from the Dyer Plateau on the AP and a stacked MSA record based on three regional ice cores (James Ross Island, Dyer Plateau and Beethoven Peninsula) (Abram et al., 2010) that reflect winter sea ice dynamics in the Bellingshausen Sea. Both records display an overall decreasing trend in MSA concentrations since 1900 CE, indicating less sea ice (Fig. 5). Another record from the Bruce Plateau ice core shows the annual net accumulation (Porter et al., 2016). The increase in snow accumulation is suggested to be linked to the sea ice extent in the Bellingshausen Sea and indicates a distinct decrease in sea ice in the second half of the 20th century, which agrees with the MSA and modeled data. All ice core records show some agreement with the mSSIC for the east Bransfield Basin (PS97/072-2) but are opposite to our biomarker records and sea ice indices for all three core sites. This is likely due to the fact that our sediment records reflect local to regional changes strongly influenced by the AP as a geographic barrier and the complex oceanography within the Bransfield Strait from interaction of BSW and WSW. As both the Dyer Plateau and the stacked MSA records are dominated by large-scale winter sea ice cover variability in the Bellingshausen Sea (centered between 70 and 100° W) (Abram et al., 2010), we suggest that the regional sea ice variability within the Bransfield Strait archived in our sediment cores is not well reflected in the ice core records.

Additionally, we took the latitudinal movement of the spring sea ice edge from modeled data (mSSIE, Fig. 5) into account, which displays a southward shift down to 63.5° S, reflecting sea ice retreat, and proposes the occasional absence of spring sea ice at all core sites since the 1970s. The spatial shift of the sea ice edge must be treated with caution because the model does not resolve regional impacts, coastal and peninsula interactions, and seasonal input of drift ice from the Weddell Sea. The MSA-based winter sea ice edge (WSIE, Fig. 5) (Abram et al., 2010) displays the same de-

creasing trend in the Bellingshausen Sea but is located 3° to the south of the modeled ice edge (from 65 to 66° S). The fact that our core sites are located north of this projected WSIE shift is another argument for why the ice core MSA cannot be considered to reflect sea ice conditions in our study area, which, according to the ice core data, would have been free of sea ice during the entire 20th century.

We relate the divergence of ice core and modeled sea ice data from our sediment core data firstly to the different spatial coverage and geographic origin of the environmental signals archived within the ice cores and secondly to the fact that AWI-ESM2 cannot resolve the AP sub-aerial and marine topography and has difficulties capturing local to regional near-coastal sea ice dynamics in the study region. In fact, our sediment records reflect the local to regional impact of the BSW and WSW that carry opposite sea ice and water mass properties and represent the sea ice properties of neither the Bellingshausen Sea nor the Weddell Sea. In addition, as the AP is acting as a geographic barrier between these water masses, the region is highly sensitive to oceanographic variabilities driven by atmospheric patterns. For example, it is suggested that strong westerly winds and a positive SAM diminish the inflow of WSW into the Bransfield Strait (Dotto et al., 2016). Although the WAP is studied quite well, the lack of high-resolution records that display local sea ice calls for further sea ice paleo-record surveys.

#### 4.4 Comparison of marine temperature proxy records with model and ice core data

Comparison of GDGT-based temperatures with modeled subsurface ocean temperature mSOT reveals a general disagreement over the 20th century (Fig. 6). Only at the Orleans Trough (PS97/068-2) does high SOT<sup>TEX</sup> reflect a possible impact of atmospheric temperatures, but as all other temperature estimations are much lower we assume that enhanced water column mixing at the Peninsula Front might diminish this effect (see Sect. 4.1). During the 19th century, SOT<sup>TEX</sup>-based cold (around the 1850s and 1900 CE) and warm events (from 1860 to 1880 CE and around 1910 CE), respectively, agree better with mSOT at all core sites than in the 20th century. SOT<sup>OH</sup> does not correspond to mSOT except since the 1990s when both data sets reflect the modern warming. SSSTs from diatoms show a short cool period around 1900 CE similar to SOT<sup>TEX</sup> and modeled data. In general, biomarker-derived temperatures point to a slight cooling trend over the last 240 years at the WAP, which fits the observed deepwater cooling between 1960 and 1990 (Ruiz Barlett et al., 2018). Simultaneously, this cooling contradicts our mSOT and observations of surface water warming that seem to be linked to the increasing positive SAM since the mid-20th century (Abram et al., 2014; Ruiz Barlett et al., 2018).

As our model includes a transient greenhouse gas forcing, the highly variable but continuously increasing mSOT (and

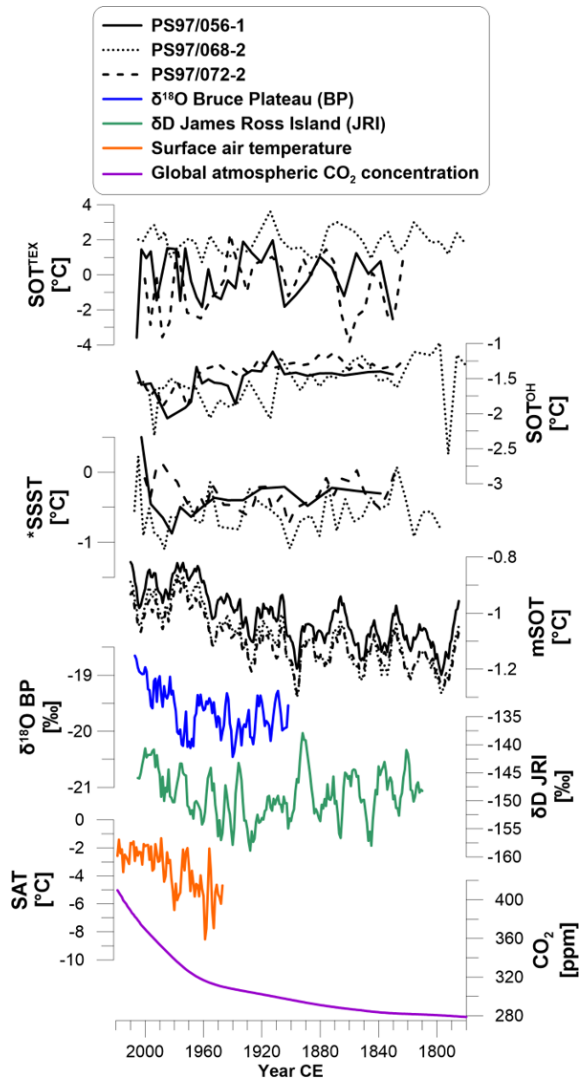


**Figure 6.** Biomarker-derived subsurface ocean temperatures based on  $\text{TEX}_{86}^L$  ( $\text{SOT}^{\text{TEX}}$ ) and hydroxylated GDGTs ( $\text{SOT}^{\text{OH}}$ ), as well as summer sea surface temperatures (SSSTs) derived from diatom assemblages compared to modeled subsurface ocean temperature (mSOT) and stable isotope ice core records from the Bruce Plateau (BP;  $\delta^{18}\text{O}$ ; 5-year running mean; Goodwin et al., 2016) and from James Ross Island (JRI;  $\delta\text{D}$ ; 5-year running mean; Abram et al., 2013). Annual mean surface air temperature (SAT) is derived from four meteorological stations (annual mean from stations O’Higgins, Faraday–Vernadsky, Bellingshausen and Jubaney; British Antarctic Survey, 2013), and global annual atmospheric carbon dioxide concentrations are combined from Meinshausen et al. (2017) and Tans and Keeling (2020). Data marked with \* are from the trigger core PS97/072-1.

mSAT) matches the observed trends in atmospheric warming derived from stable isotope ice core and meteorological data (Fig. 6). The ice core  $\delta^{18}\text{O}$  records at Bruce Plateau (Goodwin et al., 2016) and  $\delta\text{D}$  records from James Ross Island (Abram et al., 2013) display the large-scale air temperature rise in the sector of the Bellingshausen Sea and the Antarctic Peninsula region. The same upward trend is seen in mean surface air temperatures from meteorological stations on the WAP parallel to rising global atmospheric carbon dioxide concentrations (Fig. 6). However, we note that ice cores represent a large regional scale and meteorological station records are influenced by, e.g., altitude, morphology and local wind patterns, while GDGT-based ocean temperatures depict a local to regional subsurface marine record controlled by BSW and WSW. We also note that water mass transformation during sea ice cover is possible due to formation of cold, salty brine waters and enhanced vertical mixing with cold water masses (Abernathy et al., 2016). Further, sea ice melting in spring enhances the stratification of the upper water column, restricts heat exchange between the subsurface ocean and atmosphere, and could lead to a cold bias in subsurface temperature biomarker records. Nevertheless, the abrupt warming in our ocean temperature records in the 1990s follows the significant and extraordinary warming shown in air temperature records accompanied by the steep rise in atmospheric carbon dioxide.

#### 4.5 Sea ice evolution and large-scale atmospheric circulation patterns

While sediment records integrate environmental conditions of several years, the influence of highly seasonal climate modes or events may not be properly dissolved, which could explain the weaker relationships between the two. However, since atmospheric circulation affects the heat and sea ice distribution along the WAP, especially during springtime (Clem et al., 2016), we expect patterns of ENSO and/or SAM to leave a footprint in our spring sea ice IPSO<sub>25</sub> record. Several studies suggest an enhanced influence of ENSO and SAM on Antarctic temperatures with increasing greenhouse gas concentrations, so their relation to sea ice is a crucial factor for sea ice and climate predictions (Rahaman et al., 2019; Stammerjohn et al., 2008b). For example, atmosphere–ocean–sea ice interactions impact the WAP strongly through increased northerly winds during an in-phase –ENSO/+SAM mode. They lead to a strong positive feedback of atmospheric warming amplification due to shorter sea ice seasons and thinner sea ice cover with more leads permitting an enhanced heat flux from the ocean (Stammerjohn et al., 2008a). Further, positive SAM increases the presence of BSW and CDW in the Bransfield Strait and reduces the influence of WSW, resulting in higher SSTs in the Bransfield Strait (Dotto et al., 2016; Ruiz Barlett et al., 2018).

We compare IPSO<sub>25</sub> from all core sites with a tree-ring-based ENSO reconstruction (Li et al., 2013) and SAM data

from proxy records including the full mid-latitude to polar domain of the Drake Passage (Abram et al., 2014) (Fig. 7). Both ENSO and SAM have oscillating positive and negative periods, and SAM shows a slight decrease until 1860 CE. SAM and ENSO again show increases since 1930 CE and 1960 CE, respectively, and reach maximum positive states in the 2000s. When comparing biomarker and circulation patterns, SAM matches best with elevated HBI concentrations, especially at the coastal core sites, relating a higher accumulation of IPSO<sub>25</sub> to a positive SAM. During a positive SAM, stronger westerly winds cause a southward shift of the low-pressure cell over the Bellingshausen Sea and the strengthening of the polar frontal jet (Marshall et al., 2006). At this time, temperature anomalies along the WAP are very small and not even detectable at, e.g., the southwest Vernadsky–Faraday station (Marshall et al., 2006), but a remarkable “föhn” effect (Klemp and Lilly, 1975) leads to rising summer air temperatures on the eastern AP lee side. Nevertheless, our records suggest that a positive SAM is positively related to the content of IPSO<sub>25</sub> and HBI Z-triene in Bransfield Strait sediments, especially since the mid-20th century. Although a positive SAM is associated with higher SSTs due to a higher presence of BSW in the Bransfield Strait and reduced WSW (Dotto et al., 2016; Ruiz Barlett et al., 2018), we do not see any relations to our temperature proxies (Fig. S6). We suggest that a higher presence of sea ice (indicated by higher IPSO<sub>25</sub> concentrations) could lead to lower annual mean ocean temperatures because brine rejection during sea ice formation leads to cold water formation in the Bransfield Strait (Abernathy et al., 2016).

The pattern of ENSO is not related or is negatively related to biomarker concentrations in the 19th century (especially at core site PS97/072-2) and more positively in the 20th century. The recent shift to a positive ENSO is accompanied by increased IPSO<sub>25</sub> concentrations. After Yuan (2004) a positive ENSO causes sea ice advance under cold conditions in the Weddell Sea and the Bransfield Strait and warm, moist conditions in the southern Pacific Ocean. However, due to observations of recently rising atmospheric temperature (Stastna, 2010), ocean temperature (Cook et al., 2016) and declining sea ice cover along the southern WAP, a positive ENSO seems to be more likely related to warm and sea-ice-reduced conditions along the WAP in the studied period. Nevertheless, we observe that the IPSO<sub>25</sub> production at the coastal core sites (PS97/056-1 and 068-1) corresponds to positive ENSO since the 1980s. Neither SAM nor ENSO alone seems to exert a consistent control on IPSO<sub>25</sub>, phytoplankton production or ocean temperature in the Bransfield Strait (Fig. S6). A positive ENSO together and positive SAM seem to be linked to higher IPSO<sub>25</sub> concentrations, especially in the 20th century, which agrees with previous suggestions regarding the impact of atmospheric circulation patterns on sea ice conditions (Barbara et al., 2013; Etourneau et al., 2013), but as meltwater discharge seems to impact environ-

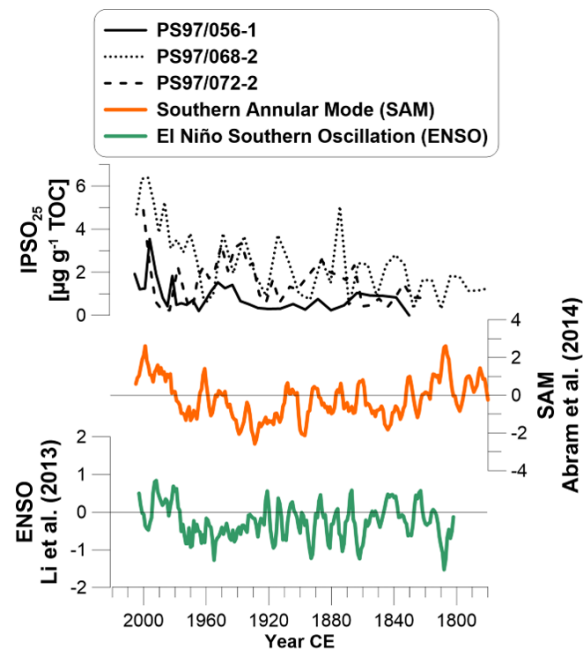


**Figure 7.** Concentrations of biomarker IPSO<sub>25</sub> in all three sediment cores compared to the circulation pattern of the Southern Annular Mode (SAM; 5-year running mean; Abram et al., 2014) and the El Niño–Southern Oscillation (ENSO; 5-year running mean; Li et al., 2013).

mental records at our near-coastal cores sites this suggestion remains hypothetical.

#### 4.6 Interpretation of combined paleoenvironmental biomarkers

While all core sites exhibit increasing concentrations of both open marine and sea ice biomarkers we simultaneously observe an ocean cooling (mainly indicated by SOT<sup>OH</sup>). We assume subsurface ocean cooling to be linked to the release of cold, salty waters during sea ice formation (Abernathy et al., 2016) and enhanced vertical mixing in winter (Frew et al., 2019) resulting from an advance of sea ice cover in the 20th century. Instead of a master stratigraphy for all three cores we defined site-specific paleoenvironmental units characterized by low, moderate and high spring sea ice cover estimates (see vertical bars in Fig. 3). Due to site-specific oceanographic characteristics, the temporal duration of the defined units may differ between the core sites. This subdivision is of qualitative nature and does not address quantified sea ice cover. It is mainly based on sea ice proxies (IPSO<sub>25</sub>, PIPSO<sub>25</sub>, WSI and *F. curta*) but also considers subsurface ocean temperatures.

- *Unit A: Low sea ice cover and high ocean temperatures.* In unit A (orange bar, Fig. 3) sea ice proxies for IPSO<sub>25</sub>, PIPSO<sub>25</sub>, WSI and *F. curta* are mostly below average and mark low winter and spring sea ice

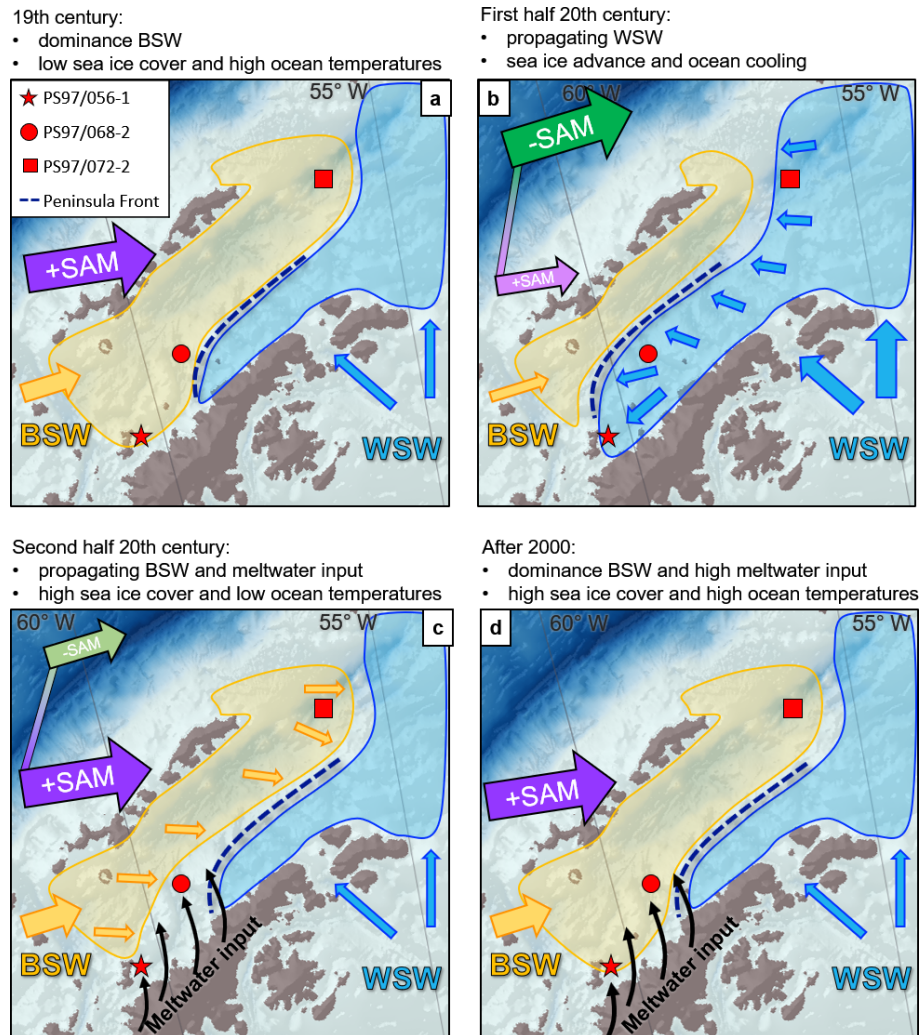


**Figure 8.** An illustration of the four environmental units and their dominant drivers of (a) low sea ice cover and high ocean temperatures from dominating BSW described in unit A, (b) moderate winter and spring sea ice cover with decreasing temperatures that propagate from the Weddell Sea to the southern WAP in unit B, (c) high but variable sea ice cover and ocean temperature lows under advancing BSW and positive SAM as well as additional meltwater pulses of unit C, and (d) high sea ice cover under a warm ocean temperature reversal as a result of BSW dominance and meltwater input from the AP in unit D. Thick and long arrows indicate a strong forcing, and thin and short arrows indicate a weak forcing. The arrows for SAM in units B and C describe the transition of the mode from the smaller to the bigger arrow.

cover accompanied by relatively high ocean temperatures ( $SOT^{OH}$ ). The sea ice minimum and probably ice-free summers occur in the mid-19th century with a remarkable WSI low at Orleans Trough (PS97/068-2) and low WSI with high HBI triene values at the east Bransfield Basin (PS97/072-2). The reduced sea ice cover could explain the relatively high subsurface ocean temperatures as a result of diminished vertical mixing (Frew et al., 2019) and enhanced input of BSW. Unit A only extends to the end of the 19th century at the two northernmost core sites, while it prolongs to the 1920s at the Trinity Island site, so we assume that the influence of BSW at the Orleans Trough and east Bransfield Basin decreases towards the 20th century. Also, a rising wind-

driven sea ice transport from the Weddell Sea (Holland and Kwok, 2012) could possibly end unit A earlier at the northernmost core sites due to a weaker westerly wind belt (Koffman et al., 2014) and a shift from positive SAM to negative SAM (Abram et al., 2014) during the 19th century.

- *Unit B: Moderate winter and spring sea ice cover with decreasing temperatures.* In unit B (green bar, Fig. 3) three of the four sea ice proxies are above average and show an increase in sea ice for both winter and spring at all core sites, in accordance with decreasing ocean temperatures. Especially at Orleans Trough (PS97/068-2), high short-term fluctuations in sea ice seem to be

common, which may relate to the interplay of water masses and a shift of the Peninsula Front, influenced by WSW in the southeast and BSW in the northwest (Fig. 1). The advance of sea ice appears about 30 years earlier at the east Bransfield Basin (PS97/072-2) than at Trinity Island (PS97/056-1) and induces a transformation towards colder subsurface ocean temperatures through brine rejection and regular sea ice melt in spring and summer (Abernathy et al., 2016). We suggest that a northward shift of the westerly wind belt with a weakening of the local winds (Koffman et al., 2014) and negative SAM (Abram et al., 2014) could have increased the influence of colder, ice-rich WSW (Dotto et al., 2016) and led to a propagation of moderate sea ice cover from northeast to southwest over several decades. The development towards moderate sea ice cover at Trinity Island since the 1920s contrasts with suggestions from Barbara et al. (2013), who interpreted near-coastal diatom assemblages and HBIs at the southern WAP to reflect decreasing sea ice cover and warmer SSTs. Therefore, we assume that the Peninsula Front might have extended southwards due to decreased westerly winds, and Trinity Island was temporarily dominated by WSW.

– *Unit C: High but variable sea ice cover and low ocean temperature.* In unit C (blue bar, Fig. 3) IPSO<sub>25</sub>, PIPSO<sub>25</sub>, WSI and *F. curta* clearly indicate the highest sea ice cover over the studied period. The majority of ocean temperature proxies show a further decrease towards low values between the 1970s and 1990s at all sites, indicating a shift towards cold, salty waters due to brine rejection from sea ice (Abernathy et al., 2016; Frew et al., 2019). In general, the high variability in sea ice cover seen in our study area matches other marine sediment records near Anvers Island (Barbara et al., 2013). These high seasonal contrasts promoted enhanced open marine biomarker production (Gonçalves-Araujo et al., 2015), evident in higher concentrations of IPSO<sub>25</sub> and HBI trienes (Figs. 3, S4) and sedimentation rates (Fig. 2) that are fueled by high nutrient release through sea ice melting (Vernet et al., 2008). All core sites experience a sudden sea ice minimum in both winter and spring and a sudden temperature rise in the 1960s at Orleans Trough (PS97/068-2), the 1970s at Trinity Island (PS97/056-1) and the 1980s at the east Bransfield Basin (PS97/072-2). This might be linked to a growing input of BSW since 1960 when SAM changes from negative to positive (Fig. 7, Abram et al., 2014) and a strengthening of the westerly winds (Bracegirdle et al., 2018). This is contrasted by a rapid advance of sea ice since the 1970s at the coastal core sites (PS97/056-1 and 68-2) that is likely driven by enhanced freshwater pulses from retreating glaciers at the AP (Cook et al., 2005; Kunz et al., 2012), which do not affect the remote east Bransfield Basin core site (PS97/072-2).

– *Unit D: High sea ice cover and warm ocean temperatures.* Unit D (purple bar, Fig. 3) is characterized by a high sea ice cover and rapidly rising ocean temperatures. The onset of this trend towards a warm subsurface ocean (Cook et al., 2016) is present at all core locations since the mid-1990s. Sea ice cover tends to increase towards maximum values in the 2000s and seems to reflect recent observations of sea ice cover rebounds in the Bellingshausen Sea and the WAP after 2005 CE (Hobbs et al., 2016; Schofield et al., 2018). At the same time the high ocean temperatures speak against cold water formation from sea ice, which lets us assume that the inflow of warm BSW is exceptionally high and dominates the temperature proxies during a strong SAM. Further, increased meltwater discharge could support sea ice formation from fresh water (Haid et al., 2017). Near Trinity Island (PS97/056-1) the drastic low of WSI and *F. curta* might show the higher sensitivity of diatoms to short-term changes compared to HBIs. Since the last unit is very short, the interpretation of warm ocean temperature together with a high sea ice cover is rather tentative. In contrast to units A to C this unit occurs simultaneously at all core sites and marks an environmental change on a larger scale that overprints the former strong local impacts.

From the temporal onset of different environmental states in the Bransfield Strait we interpret sea ice and ocean temperature distributions as mainly the result of the interplay between BWS and WSW that is controlled by westerly winds and SAM. The influence of these water masses was potentially overprinted by meltwater discharge at the coastal core sites in the second half of the 20th century. Figure 8a illustrates how a mainly positive SAM and the dominance of BSW lead to the low sea ice cover in the Bransfield Strait describing unit A. In unit B, a shift from positive SAM to negative SAM in the first half of the 20th century supports a sea ice advance first at the core sites that are closest to the WSW (PS97/68-2 and 72-2) and later at the southernmost core site (PS97/056-1) (Fig. 8b). With a positive SAM in the 1960s a short-term sea ice minimum appears from the southwest to the northeast, indicating the growing dominance of BSW (Fig. 8c). Despite a shift towards positive SAM and the rising dominance of BSW in the following decades, sea ice advance and low ocean temperatures occur at the coastal core sites defining unit C. We assume this to be a strong imprint of meltwater input, which promotes sea ice formation because of a higher freezing point. The meltwater originates from fast-retreating glacier fronts and glacial melting since the 1980s (Cook et al., 2005) due to rising greenhouse gases and atmospheric temperatures (Fig. 6). The rise in ocean temperatures in unit D might relate to the establishment of positive SAM and continuous input from BSW (Fig. 8d). Since the 2000s, glacial melting increased significantly (Rignot et al., 2019), and this enhanced freshwater input may have in-

creased the sea ice extent. It is also likely that biomarker production in both sea ice and open marine environments benefits from a sudden sea ice retreat (as was recorded by satellites for 2000 to 2005; Fig. 4) due to thinner sea ice (Hancke et al., 2018) and a higher nutrient overturn by sea ice melting (Vernet et al., 2008).

From our reconstructions of sea ice and ocean temperatures we argue that SAM was the main driver of water mass distribution in the Bransfield Strait in the past 240 years, as was also found in studies covering the last 40 years (Clem et al., 2016; Dotto et al., 2016; Stammerjohn et al., 2008b; Yuan, 2004), but local input from meltwater is able to increase near-coastal sea ice formation (and related primary production) during sea-ice-diminishing conditions, which can overprint the dominating climate mode. This may explain why the positive relation between positive SAM and IPSO<sub>25</sub> concentrations is the highest at the near-coastal core sites, although positive SAM would lead to a higher BSW inflow and a reduction of sea ice.

## 5 Summary and conclusions

We analyzed the spring sea ice biomarker IPSO<sub>25</sub> and other biomarkers as well as diatom assemblages in three sediment cores from the Bransfield Strait covering the past 240 years and combined our results with numerical model data, satellite observations, temperature records and paleorecords of atmospheric circulation patterns. We note that the interpretation of the biomarker data for past sea ice estimates in Antarctica is strongly impacted by the origin of water masses, mixing, nutrient input and dynamics of sea-ice-related primary production. While IPSO<sub>25</sub> concentrations agree with satellite sea ice data, they seem to contradict the long-term large-scale ice core and model data. We note that the significance of our coupled climate model is limited due to the complex oceanography in the Bransfield Strait that is controlled by atmospheric circulation patterns and forced by enhanced glacial melting during the past 50 years. We also emphasize the fact that local coastal influences, high sea ice dynamics and thinner sea ice, promoting the production of both sea ice diatoms and open marine phytoplankton, may affect the interpretation of IPSO<sub>25</sub> and the sea ice index PIPSO<sub>25</sub>. When estimating spring sea ice cover, the strong sensitivity of IPSO<sub>25</sub> to local influences such as water masses, coastal interaction and, e.g., a higher sea ice algae productivity resulting from thinner ice cover need to be taken into account. We hence recommend considering additional phytoplankton data instead of constructing sea ice estimates based solely on IPSO<sub>25</sub> and PIPSO<sub>25</sub> records.

Although ENSO and SAM are postulated to influence sea ice and heat distribution in the Bransfield Strait, our biomarker data do not show a clear relationship between the long-term ocean temperature development and these patterns as has been suggested from recent studies. However, ENSO

and/or SAM both seem to affect the sea ice regime in the Bransfield Strait. Based on sea ice biomarkers and sea ice indices, we roughly divided the 240-year records into four environmental units with different timings (Fig. 8):

- *low sea ice cover and high ocean temperatures* due to a dominance of warm BSW during a positive SAM in the 19th century (Fig. 8a);
- *moderate winter and spring sea ice cover with decreasing temperatures* when positive SAM shifts towards negative SAM and the input of colder and sea-ice-rich WSW in the Bransfield Strait increases (Fig. 8b);
- *high but variable sea ice cover and low ocean temperature* established over several decades, propagating from the northeast to the southwest, with a change from negative SAM to positive SAM and diverging sea ice conditions between the offshore and coastal core sites due to glacial melting and meltwater input (Fig. 8c);
- *high sea ice cover and warm ocean temperatures* related to a peak of positive SAM and BSW input during a short interruption of atmospheric warming and glacial melting (Fig. d).

We conclude that the different timing of the units mirrors the decadal change in dominating water masses at every core site. A dominance of positive SAM promoted the enhanced input of BSW in the Bransfield Strait that led to a sea ice reduction at the remote core site (unit C, Fig. 8c). In contradiction to that, sea ice cover was enhanced at the near-coastal core sites due to a strong overprint from enhanced meltwater input from glaciers since the 1960s, and ocean cooling resulted from cold brine rejections during sea ice formation.

**Data availability.** All data are available through the open-access repository on the Pangaea website at <https://www.pangaea.de/> (<https://doi.org/10.1594/PANGAEA.918808>, Vorrath et al., 2020).

**Supplement.** The supplement related to this article is available online at: <https://doi.org/10.5194/cp-16-2459-2020-supplement>.

**Author contributions.** The study was conceived by MEV and JM. Data collections and experimental investigations were done by MEV together with PC, LR, PM and CBL (sampling, diatoms, dating); WG (dating); OE (diatom transfer functions); JM and GM (HBIs, GDGTs); XS and GL (modeling and Fig. S3); CH (satellite sea ice data); and TO (ice cores). MEV drafted the paper and figures. JM supervised the study. All authors contributed to the interpretation and discussion of the results as well as the conclusion of this study.

**Competing interests.** The authors declare that they have no conflict of interest.

**Special issue statement.** This article is part of the special issue “Reconstructing Southern Ocean sea-ice dynamics on glacial-to-historical timescales”. It is not associated with a conference.

**Acknowledgements.** We thank the captain, crew and chief scientist, Frank Lamy, of RV *Polarstern* cruise PS97. Denise Diekstaal, Jens Hefter, Ingrid Stimac, Alejandro Avila and Ruth Cordelair are thanked for their laboratory support. We also thank Andrés Cádiz for the help on diatom slide preparations and counts on core PS97/056-1. Simon Belt is acknowledged for providing the 7-HND internal standard for HBI quantification. Financial support was provided through the Helmholtz research grant VH-NG-1101 and the Helmholtz Excellence Network “The Polar System and its Effects on the Ocean Floor” ExNet-0001. Partial financial support from the Research Center Dynamics of High Latitude Marine Ecosystems (FONDAP-IDEAL 15150003, Chile) and the Center for Oceanographic Research COPAS Sur-Austral (AFB170006, Chile) is acknowledged. We thank two anonymous reviewers for their constructive comments that helped us to improve the paper.

**Financial support.** This research has been supported by a Helmholtz research grant (grant no. VH-NG-1101), the IDEAL Center (FONDAP grant no. 15150003), and the Helmholtz Excellence Network “The Polar System and its Effects on the Ocean Floor” (grant no. ExNet-0001).

The article processing charges for this open-access publication were covered by a Research Centre of the Helmholtz Association.

**Review statement.** This paper was edited by Marit-Solveig Seidenkrantz and reviewed by two anonymous referees.

## References

- Abernathy, R. P., Cerovecki, I., Holland, P. R., Newsom, E., Mazloff, M., and Talley, L. D.: Water-mass transformation by sea ice in the upper branch of the Southern Ocean overturning, *Nat. Geosci.*, 9, 596–601, <https://doi.org/10.1038/ngeo2749>, 2016.
- Abram, N. J., Thomas, E. R., McConnell, J. R., Mulvaney, R., Bracegirdle, T. J., Sime, L. C., and Aristarain, A. J.: Ice core evidence for a 20th century decline of sea ice in the Bellingshausen Sea, Antarctica, *J. Geophys. Res.*, 115, D23101, <https://doi.org/10.1029/2010JD014644>, 2010.
- Abram, N. J., Mulvaney, R., Wolff, E. W., Triest, J., Kipfstuhl, S., Trusel, L. D., Vimeux, F., Fleet, L., and Arrowsmith, C.: Acceleration of snow melt in an Antarctic Peninsula ice core during the twentieth century, *Nat. Geosci.*, 6, 404–411, <https://doi.org/10.1038/ngeo1787>, 2013.
- Abram, N. J., Mulvaney, R., Vimeux, F., Phipps, S. J., Turner, J., and England, M. H.: Evolution of the Southern Annular Mode during the past millennium, *Nat. Clim. Change*, 4, 564–569, <https://doi.org/10.1038/nclimate2235>, 2014.
- Alexander, V. and Niebauer, H.: Oceanography of the eastern Bering Sea ice-edge zone in spring, *Limn.*, 26, 1111–1125, 1981.
- Allen, C. S.: Proxy development: a new facet of morphological diversity in the marine diatom *Eucampia antarctica* (Castracane) Mangin, *J. Micropalaeontol.*, 33, 131–142, <https://doi.org/10.1144/jmpaleo2013-025>, 2014.
- Allison, I., Tivendale, C. M., Akerman, G. J., Tann, J. M., and Wills, R. H.: Seasonal Variations In The Surface Energy Exchanges Over Antarctic Sea Ice and Coastal Waters, *Ann. Glaciol.*, 3, 12–16, <https://doi.org/10.3189/S0260305500002445>, 1982.
- Appleby, P. G. and Oldfield, F.: The calculation of lead-210 dates assuming a constant rate of supply of unsupported 210Pb to the sediment, *CATENA*, 5, 1–8, [https://doi.org/10.1016/S0341-8162\(78\)80002-2](https://doi.org/10.1016/S0341-8162(78)80002-2), 1978.
- Armand, L. K. and Zielinski, U.: DIATOM SPECIES OF THE GENUS *RHIZOSOLENIA* FROM SOUTHERN OCEAN SEDIMENTS: DISTRIBUTION AND TAXONOMIC NOTES, *Diatom Res.*, 16, 259–294, <https://doi.org/10.1080/0269249X.2001.9705520>, 2001.
- Arrigo, K. R., Worthen, D. L., Lizotte, M. P., Dixon, P., and Dieckmann, G.: Primary Production in Antarctic Sea Ice, *Science*, 276, 394–397, <https://doi.org/10.1126/science.276.5311.394>, 1997.
- Barbara, L., Crosta, X., Schmidt, S., and Massé, G.: Diatoms and biomarkers evidence for major changes in sea ice conditions prior the instrumental period in Antarctic Peninsula, *Quaternary Sci. Rev.*, 79, 99–110, <https://doi.org/10.1016/j.quascirev.2013.07.021>, 2013.
- Belt, S. T. and Müller, J.: The Arctic sea ice biomarker IP 25?: a review of current understanding, recommendations for future research and applications in palaeo sea ice reconstructions, *Quaternary Sci. Rev.*, 79, 9–25, <https://doi.org/10.1016/j.quascirev.2012.12.001>, 2013.
- Belt, S. T., Allard, W. G., Massé, G., Robert, J. M., and Rowland, S. J.: Highly branched isoprenoids (HBIs): Identification of the most common and abundant sedimentary isomers, *Geochim. Cosmochim. Ac.*, 64, 3839–3851, [https://doi.org/10.1016/S0016-7037\(00\)00464-6](https://doi.org/10.1016/S0016-7037(00)00464-6), 2000.
- Belt, S. T., Brown, T. A., Ringrose, A. E., Cabedo-Sanz, P., Mundy, C. J., Gosselin, M., and Poulin, M.: Quantitative measurement of the sea ice diatom biomarker IP25 and sterols in Arctic sea ice and underlying sediments: Further considerations for palaeo sea ice reconstruction, *Org. Geochem.*, 62, 33–45, <https://doi.org/10.1016/J.ORGEOCHEM.2013.07.002>, 2013.
- Belt, S. T., Brown, T. A., Ampel, L., Cabedo-Sanz, P., Fahl, K., Kocis, J. J., Massé, G., Navarro-Rodriguez, A., Ruan, J., and Xu, Y.: An inter-laboratory investigation of the Arctic sea ice biomarker proxy IP25 in marine sediments: key outcomes and recommendations, *Clim. Past*, 10, 155–166, <https://doi.org/10.5194/cp-10-155-2014>, 2014.
- Belt, S. T., Smik, L., Brown, T. A., Kim, J. H., Rowland, S. J., Allen, C. S., Gal, J. K., Shin, K. H., Lee, J. I., and Taylor, K. W. R.: Source identification and distribution reveals the potential of the geochemical Antarctic sea ice proxy IPSO25, *Nat. Commun.*, 7, 1–10, <https://doi.org/10.1038/ncomms12655>, 2016.
- Belt, S. T., Brown, T. A., Smik, L., Tatarek, A., Wiktor, J., Stowasser, G., Assmy, P., Allen, C. S., and Husum, K.: Identification of C<sub>25</sub> highly branched isoprenoid (HBI) alkenes in diatoms of the genus *Rhizosolenia* in polar and sub-polar marine phytoplankton, *Org. Geochem.*, 110, 65–72, <https://doi.org/10.1016/j.orggeochem.2017.05.007>, 2017.

- Berger, A. L.: Long-Term Variations of Daily Insolation and Quaternary Climate Changes, *J. Atmos. Sci.*, 35, 2362–2367, 1978.
- Bevington, P. R., Robinson, D. K., and Bunce, G.: Data Reduction and Error Analysis for the Physical Sciences, 2nd ed., *Am. J. Phys.*, 61, 766–767, <https://doi.org/10.1119/1.17439>, 1993.
- Blaauw, M.: Methods and code for ‘classical’ age-modelling of radiocarbon sequences, *Quat. Geochronol.*, 5, 512–518, <https://doi.org/10.1016/J.QUAGEO.2010.01.002>, 2010.
- Bodas-Salcedo, A., Williams, K. D., Ringer, M. A., Beau, I., Cole, J. N. S., Dufresne, J.-L., Koshiro, T., Stevens, B., Wang, Z., and Yokohata, T.: Origins of the Solar Radiation Biases over the Southern Ocean in CFMIP2 Models\*, *J. Climate*, 27, 41–56, <https://doi.org/10.1175/JCLI-D-13-00169.1>, 2014.
- Bracegirdle, T. J., Stephenson, D. B., Turner, J., and Phillips, T.: The importance of sea ice area biases in 21st century multimodel projections of Antarctic temperature and precipitation, *Geophys. Res. Lett.*, 42, 832–839, <https://doi.org/10.1002/2015GL067055>, 2015.
- Bracegirdle, T. J., Hyder, P., and Holmes, C. R.: CMIP5 Diversity in Southern Westerly Jet Projections Related to Historical Sea Ice Area: Strong Link to Strengthening and Weak Link to Shift, *J. Climate*, 31, 195–211, <https://doi.org/10.1175/JCLI-D-17-0320.1>, 2018.
- Bracegirdle, T. J., Colleoni, F., Abram, N. J., Bertler, N. A. N., Dixon, D. A., England, M., Favier, V., Fogwill, C. J., Fyfe, J. C., Goodwin, I., Goosse, H., Hobbs, W., Jones, J. M., Keller, E. D., Khan, A. L., Phipps, S. J., Raphael, M. N., Russell, J., Sime, L., Thomas, E. R., van den Broeke, M. R., and Wainer, I.: Back to the Future: Using Long-Term Observational and Paleo-Proxy Reconstructions to Improve Model Projections of Antarctic Climate, *Geosciences*, 9, 255, <https://doi.org/10.3390/geosciences9060255>, 2019.
- British Antarctic Survey: UK Antarctic Surface, Surface meteorology at British Antarctic Survey Stations, British Antarctic Survey, NERC, 1947–2013, <https://doi.org/10.5285/569d53fb-9b90-47a6-b3ca-26306e696706>, 2013.
- Buffen, A., Leventer, A., Rubin, A., and Hutchins, T.: Diatom assemblages in surface sediments of the northwestern Weddell Sea, *Antarctic Peninsula, Mar. Micropaleontol.*, 62, 7–30, <https://doi.org/10.1016/J.MARMICRO.2006.07.002>, 2007.
- Burckle, L. H. and Cooke, D. W.: Late Pleistocene *Eucampia antarctica* Abundance Stratigraphy in the Atlantic Sector of the Southern Ocean, *Micropaleontology*, 29, 6–10, <https://doi.org/10.2307/1485648>, 1983.
- Butterworth, B. J. and Miller, S. D.: Air-sea exchange of carbon dioxide in the Southern Ocean and Antarctic marginal ice zone, *Geophys. Res. Lett.*, 43, 7223–7230, <https://doi.org/10.1002/2016GL069581>, 2016.
- Campagne, P., Crosta, X., Schmidt, S., Noëlle Houssais, M., Ther, O., and Massé, G.: Sedimentary response to sea ice and atmospheric variability over the instrumental period off Adélie Land, East Antarctica, *Biogeosciences*, 13, 4205–4218, <https://doi.org/10.5194/bg-13-4205-2016>, 2016.
- Canals, M. and Amblas, D.: Seafloor kettle holes in Orleans Trough, Bransfield Basin, Antarctic Peninsula, *Geological Society, London, Memoirs*, 46, 313–314, <https://doi.org/10.1144/M46.16>, 2016a.
- Canals, M. and Amblas, D.: The bundle: a mega-scale glacial landform left by an ice stream, *Western Bransfield Basin, Geological Society, London, Memoirs*, 46, 177–178, <https://doi.org/10.1144/M46.157>, 2016b.
- Canals, M., Amblas, D., and Casamor, J. L.: Cross-shelf troughs in Central Bransfield Basin, Antarctic Peninsula, *Geological Society, London, Memoirs*, 46, 171–172, <https://doi.org/10.1144/M46.138>, 2016.
- Cárdenas, P., Lange, C. B., Vernet, M., Esper, O., Srain, B., Vorrath, M.-E., Ehrhardt, S., Müller, J., Kuhn, G., Arz, H. W. H. W. H. W., Lembke-Jene, L., Lamy, F., Cárdenas, P., Lange, C. B., Vernet, M., Esper, O., Srain, B., Vorrath, M.-E., Ehrhardt, S., Müller, J., Kuhn, G., Arz, H. W., Lester Lembke-Jene, F. L.: Biogeochemical proxies and diatoms in surface sediments across the Drake Passage reflect oceanic domains and frontal systems in the region, *Prog. Oceanogr.*, 174, 72–88, <https://doi.org/10.1016/j.pocean.2018.10.004>, 2019.
- Cavalieri, D. J., Parkinson, C. L., Gloersen, P., and Zwally, H. J.: Sea Ice Concentrations from Nimbus-7 SMMR and DMSP SSM/I-SSMIS Passive Microwave Data, Version 1, Boulder, Colorado, USA, <https://doi.org/10.5067/8GQ8LZQVLOVL>, 1996.
- Cefarelli, A. O., Ferrario, M. E., Almandoz, G. O., Atencio, A. G., Akselman, R., and Vernet, M.: Diversity of the diatom genus *Fragilariopsis* in the Argentine Sea and Antarctic waters: morphology, distribution and abundance, *Polar Biol.*, 33, 1463–1484, <https://doi.org/10.1007/s00300-010-0794-z>, 2010.
- Clem, K. R., Renwick, J. A., McGregor, J., and Fogt, R. L.: The relative influence of ENSO and SAM on Antarctic Peninsula climate, *J. Geophys. Res.-Atmos.*, 121, 9324–9341, <https://doi.org/10.1002/2016JD025305>, 2016.
- Collares, L. L., Mata, M. M., Kerr, R., Arigony-Neto, J., and Barbat, M. M.: Iceberg drift and ocean circulation in the northwestern Weddell Sea, *Antarctica, Deep Sea Research Part II: Topical Studies in Oceanography*, 149, 10–24, <https://doi.org/10.1016/j.dsr2.2018.02.014>, 2018.
- Cook, A. J., Fox, A. J., Vaughan, D. G., and Ferrigno, J. G.: Retreating glacier fronts on the Antarctic Peninsula over the past half-century, *Science*, 308, 541–544, <https://doi.org/10.1126/science.1104235>, 2005.
- Cook, A. J., Holland, P. R., Meredith, M. P., Murray, T., Luckman, A., and Vaughan, D. G.: Ocean forcing of glacier retreat in the western Antarctic Peninsula, *Science*, 353, 283–286, <https://doi.org/10.1126/science.aae0017>, 2016.
- Crosta, X., Pichon, J.-J., and Burckle, L. H.: Application of modern analog technique to marine Antarctic diatoms: Reconstruction of maximum sea-ice extent at the Last Glacial Maximum, *Paleoceanography*, 13, 284–297, <https://doi.org/10.1029/98PA00339>, 1998.
- Crosta, X., Sturm, A., Armand, L., and Pichon, J.-J.: Late Quaternary sea ice history in the Indian sector of the Southern Ocean as recorded by diatom assemblages, *Mar. Micropaleontol.*, 50, 209–223, [https://doi.org/10.1016/S0377-8398\(03\)00072-0](https://doi.org/10.1016/S0377-8398(03)00072-0), 2004.
- Danilov, S., Sidorenko, D., Wang, Q., and Jung, T.: The Finite-volume Sea ice–Ocean Model (FESOM2), *Geosci. Model Dev.*, 10, 765–789, <https://doi.org/10.5194/gmd-10-765-2017>, 2017.
- Ding, Q., Steig, E. J., Battisti, D. S., and Wallace, J. M.: Influence of the tropics on the southern annular mode, *J. Climate*, 25, 6330–6348, <https://doi.org/10.1175/JCLI-D-11-00523.1>, 2012.
- Dotto, T. S., Kerr, R., Mata, M. M., and Garcia, C. A. E.: Multidecadal freshening and lightening in the deep waters of the

- Bransfield Strait, Antarctica, *J. Geophys. Res.-Oceans*, 121, 3741–3756, <https://doi.org/10.1002/2015JC011228>, 2016.
- Esper, O. and Gersonde, R.: New tools for the reconstruction of Pleistocene Antarctic sea ice, *Palaeogeogr. Palaeoclimatol.*, 399, 260–283, <https://doi.org/10.1016/j.palaeo.2014.01.019>, 2014a.
- Esper, O. and Gersonde, R.: Quaternary surface water temperature estimations: New diatom transfer functions for the Southern Ocean, *Palaeogeogr. Palaeoclimatol.*, 414, 1–19, <https://doi.org/10.1016/j.palaeo.2014.08.008>, 2014b.
- Esper, O., Gersonde, R., and Kadagies, N.: Diatom distribution in southeastern Pacific surface sediments and their relationship to modern environmental variables, *Palaeogeogr. Palaeoclimatol.*, 287, 1–27, <https://doi.org/10.1016/j.palaeo.2009.12.006>, 2010.
- Etourneau, J., Collins, L. G., Willmott, V., Kim, J.-H., Barbara, L., Leventer, A., Schouten, S., Sinninghe Damsté, J. S., Bianchini, A., Klein, V., Crosta, X., and Massé, G.: Holocene climate variations in the western Antarctic Peninsula: evidence for sea ice extent predominantly controlled by changes in insolation and ENSO variability, *Clim. Past*, 9, 1431–1446, <https://doi.org/10.5194/cp-9-1431-2013>, 2013.
- Etourneau, J., Sgubin, G., Crosta, X., Swingedouw, D., Willmott, V., Barbara, L., Houssais, M. N., Schouten, S., Damsté, J. S. S., Goosse, H., Escutia, C., Crespin, J., Massé, G., and Kim, J. H.: Ocean temperature impact on ice shelf extent in the eastern Antarctic Peninsula, *Nat. Commun.*, 10, 8–15, <https://doi.org/10.1038/s41467-018-08195-6>, 2019.
- Fietz, S., Huguet, C., Rueda, G., Hambach, B., and Rosell-Melé, A.: Hydroxylated isoprenoidal GDGTs in the Nordic Seas, *Mar. Chem.*, 152, 1–10, <https://doi.org/10.1016/j.marchem.2013.02.007>, 2013.
- Fietz, S., Ho, S. L., Huguet, C., Rosell-Melé, A., and Martínez-García, A.: Appraising GDGT-based seawater temperature indices in the Southern Ocean, *Org. Geochem.*, 102, 93–105, <https://doi.org/10.1016/j.orggeochem.2016.10.003>, 2016.
- Fietz, S., Ho, S. L., and Huguet, C.: Archaeal Membrane Lipid-Based Paleothermometry for Applications in Polar Oceans, *Oceanography*, 33, 104–114, <https://doi.org/10.5670/oceanog.2020.207>, 2020.
- Flynn, W. W.: The determination of low levels of polonium-210 in environmental materials, *Anal. Chim. Acta*, 43, 221–227, [https://doi.org/10.1016/S0003-2670\(00\)89210-7](https://doi.org/10.1016/S0003-2670(00)89210-7), 1968.
- Frants, M., Gille, S. T., Hewes, C. D., Holm-Hansen, O., Kahru, M., Lombrozo, A., Measures, C. I., Mitchell, G. B., Wang, H., and Zhou, M.: Optimal multiparameter analysis of source water distributions in the Southern Drake Passage, *Deep Sea Research Part II: Topical Studies in Oceanography*, 90, 31–42, <https://doi.org/10.1016/j.dsr2.2012.06.002>, 2013.
- Frew, R. C., Feltham, D. L., Holland, P. R., and Petty, A. A.: Sea ice – ocean feedbacks in the antarctic shelf seas, *J. Phys. Oceanogr.*, 49, 2423–2446, <https://doi.org/10.1175/JPO-D-18-0229.1>, 2019.
- Gersonde, R. and Zielinski, U.: The reconstruction of late Quaternary Antarctic sea-ice distribution – the use of diatoms as a proxy for sea-ice, *Palaeogeogr. Palaeoclimatol. Palaeoecol.*, 162, 263–286, [https://doi.org/10.1016/S0031-0182\(00\)00131-0](https://doi.org/10.1016/S0031-0182(00)00131-0), 2000.
- Gersonde, R., Crosta, X., Abelmann, A., and Armand, L.: Sea-surface temperature and sea ice distribution of the Southern Ocean at the EPILOG Last Glacial Maximum – a circum-Antarctic view based on siliceous microfossil records, *Quaternary Sci. Rev.*, 24, 869–896, <https://doi.org/10.1016/j.quascirev.2004.07.015>, 2005.
- Gloersen, P., Campbell, W. J., Cavalieri, D. J., Comiso, J. C., Parkinson, C. L., and Zwally, H. J.: Arctic and antarctic sea ice, 1978, *Ann. Glaciol.*, 17, 149–154, 1993.
- Gonçalves-Araujo, R., de Souza, M. S., Tavano, V. M., and Garcia, C. A. E.: Influence of oceanographic features on spatial and interannual variability of phytoplankton in the Bransfield Strait, Antarctica, *J. Mar. Syst.*, 142, 1–15, <https://doi.org/10.1016/j.jmarsys.2014.09.007>, 2015.
- Goodwin, B. P., Mosley-Thompson, E., Wilson, A. B., Porter, S. E., and Sierra-Hernandez, M. R.: Accumulation Variability in the Antarctic Peninsula: The Role of Large-Scale Atmospheric Oscillations and Their Interactions, *J. Climate*, 29, 2579–2596, <https://doi.org/10.1175/JCLI-D-15-0354.1>, 2016.
- Haid, V., Iovino, D., and Masina, S.: Impacts of freshwater changes on Antarctic sea ice in an eddy-permitting sea-ice–ocean model, *The Cryosphere*, 11, 1387–1402, <https://doi.org/10.5194/tc-11-1387-2017>, 2017.
- Hancke, K., Lund-Hansen, L. C., Lamare, M. L., Højlund Pedersen, S., King, M. D., Andersen, P., and Sorrell, B. K.: Extreme Low Light Requirement for Algae Growth Underneath Sea Ice: A Case Study From Station Nord, NE Greenland, *J. Geophys. Res.-Oceans*, 123, 985–1000, <https://doi.org/10.1002/2017JC013263>, 2018.
- Hellmer, H. H., Kauker, F., Timmermann, R., Determann, J., and Rae, J.: Twenty-first-century warming of a large Antarctic ice-shelf cavity by a redirected coastal current, *Nature*, 485, 225–228, <https://doi.org/10.1038/nature11064>, 2012.
- Hobbs, W. R., Massom, R., Stammerjohn, S., Reid, P., Williams, G., and Meier, W.: A review of recent changes in Southern Ocean sea ice, their drivers and forcings, *Global Planet. Change*, 143, 228–250, <https://doi.org/10.1016/j.gloplacha.2016.06.008>, 2016.
- Hofmann, E. E., Klinck, J. M., Lascara, C. M., and Smith, D. A.: Water mass distribution and circulation west of the Antarctic Peninsula and including Bransfield Strait, *American Geophysical Union*, 61–80, <https://doi.org/10.1029/AR070p0061>, 1996.
- Holland, P. R. and Kwok, R.: Wind-driven trends in Antarctic sea-ice drift, *Nat. Geosci.*, 5, 872–875, <https://doi.org/10.1038/ngeo1627>, 2012.
- Hopmans, E. C., Weijers, J. W. H., Schefuß, E., Herfort, L., Sinninghe Damsté, J. S., and Schouten, S.: Variability in the Benguela Current upwelling system over the past 70,000 years, *Earth Planet. Sci. Lett.*, 224, 107–116, <https://doi.org/10.1016/j.epsl.2004.05.012>, 2004.
- Huguet, C., Fietz, S., and Rosell-Melé, A.: Global distribution patterns of hydroxy glycerol dialkyl glycerol tetraethers, *Org. Geochem.*, 57, 107–118, <https://doi.org/10.1016/j.orggeochem.2013.01.010>, 2013.
- Huss, M. and Farinotti, D.: A high-resolution bedrock map for the Antarctic Peninsula, *The Cryosphere*, 8, 1261–1273, <https://doi.org/10.5194/tc-8-1261-2014>, 2014.
- Ingólfsson, Ó., Hjort, C., and Humlum, O.: Glacial and Climate History of the Antarctic Peninsula since the Last Glacial Maximum, *Arct. Antarct. Alp. Res.*, 35, 175–186, [https://doi.org/10.1657/1523-0430\(2003\)035\[0175:GACHOT\]2.0.CO;2](https://doi.org/10.1657/1523-0430(2003)035[0175:GACHOT]2.0.CO;2), 2003.
- IPCC: Summary for Policymakers, edited by: Masson-Delmotte, V., Zhai, P., Pörtner, H.-O., Roberts, D., Skea, J., Shukla, P. R.,

- Pirani, A., Moufouma-Okia, W., Péan, C., Pidcock, R., Connors, S., Matthews, J. B. R., Chen, Y., Zhou, X., Gomis, M. I., Lonnoy, E., Maycock, T., Tignor, M., and Waterfield, T., available at: [https://www.ipcc.ch/site/assets/uploads/sites/2/2019/05/SR15\\_SPM\\_version\\_report\\_LR.pdf](https://www.ipcc.ch/site/assets/uploads/sites/2/2019/05/SR15_SPM_version_report_LR.pdf) (last access: 23 April 2020) 2018.
- IPCC: Summary for Policymakers, in: IPCC Special Report on the Ocean and Cryosphere in a Changing Climate, edited by: Pörtner, H. O., Roberts, D. C., Masson-Delmotte, V., Zhai, P., Tignor, M., Poloczanska, E., Mintebek, K., Nicolai, M., Okem, A., Petzold, J., Rama, B., and Weyer, N., available at: [https://report.ipcc.ch/srocc/pdf/SROCC\\_SPM\\_Approved.pdf](https://report.ipcc.ch/srocc/pdf/SROCC_SPM_Approved.pdf) (last access: 23 April 2020), 2019.
- Jones, J. M., Gille, S. T., Goosse, H., Abram, N. J., Canziani, P. O., Charman, D. J., Clem, K. R., Crosta, X., de Lavergne, C., Eisenman, I., England, M. H., Fogt, R. L., Frankcombe, L. M., Marshall, G. J., Masson-Delmotte, V., Morrison, A. K., Orsi, A. J., Raphael, M. N., Renwick, J. A., Schneider, D. P., Simpkins, G. R., Steig, E. J., Stenni, B., Swingedouw, D., and Vance, T. R.: Assessing recent trends in high-latitude Southern Hemisphere surface climate, *Nat. Clim. Change*, 6, 917–926, <https://doi.org/10.1038/nclimate3103>, 2016.
- Kalanetra, K. M., Bano, N., and Hollibaugh, J. T.: Ammonia-oxidizing Archaea in the Arctic Ocean and Antarctic coastal waters, *Environ. Microbiol.*, 11, 2434–2445, <https://doi.org/10.1111/j.1462-2920.2009.01974.x>, 2009.
- Kim, D., Kim, D. Y., Kim, Y. J., Kang, Y. C., and Shim, J.: Downward fluxes of biogenic material in Bransfield Strait, *Antarct. Sci.*, 16, 227–237, <https://doi.org/10.1017/S0954102004002032>, 2004.
- Kim, J.-H., van der Meer, J., Schouten, S., Helmke, P., Willmott, V., Sangiorgi, F., Koç, N., Hopmans, E. C., and Damsté, J. S. S.: New indices and calibrations derived from the distribution of cretaceous isoprenoid tetraether lipids: Implications for past sea surface temperature reconstructions, *Geochim. Cosmochim. Ac.*, 74, 4639–4654, <https://doi.org/10.1016/j.gca.2010.05.027>, 2010.
- Kim, J.-H., Crosta, X., Willmott, V., Renssen, H., Bonnin, J., Helmke, P., Schouten, S., and Sinninghe Damsté, J. S.: Holocene subsurface temperature variability in the eastern Antarctic continental margin, *Geophys. Res. Lett.*, 39, L06705, <https://doi.org/10.1029/2012GL051157>, 2012.
- Klemp, J. B. and Lilly, D. R.: The Dynamics of Wave-Induced Downslope Winds, *J. Atmos. Sci.*, 32, 320–339, [https://doi.org/10.1175/1520-0469\(1975\)032<0320:TADOWID>2.0.CO;2](https://doi.org/10.1175/1520-0469(1975)032<0320:TADOWID>2.0.CO;2), 1975.
- Klunder, M. B., Laan, P., De Baar, H. J. W., Middag, R., Neven, I., and Van Ooijen, J.: Dissolved Fe across the Weddell Sea and Drake Passage: impact of DFe on nutrient uptake, *Biogeochemistry*, 11, 651–669, <https://doi.org/10.5194/bg-11-651-2014>, 2014.
- Koffman, B. G., Kreutz, K. J., Breton, D. J., Kane, E. J., Winski, D. A., Birkel, S. D., Kurbatov, A. V., and Handley, M. J.: Centennial-scale variability of the Southern Hemisphere westerly wind belt in the eastern Pacific over the past two millennia, *Clim. Past*, 10, 1125–1144, <https://doi.org/10.5194/cp-10-1125-2014>, 2014.
- Köhler, P., Nehrbass-Ahles, C., Schmitt, J., Stocker, T. F., and Fischer, H.: A 156 kyr smoothed history of the atmospheric greenhouse gases CO<sub>2</sub>, CH<sub>4</sub>, and N<sub>2</sub>O and their radiative forcing, *Earth Syst. Sci. Data*, 9, 363–387, <https://doi.org/10.5194/essd-9-363-2017>, 2017.
- Kunz, M., King, M. A., Mills, J. P., Miller, P. E., Fox, A. J., Vaughan, D. G., and Marsh, S. H.: Multi-decadal glacier surface lowering in the Antarctic Peninsula, *Geophys. Res. Lett.*, 39, L19502, <https://doi.org/10.1029/2012GL052823>, 2012.
- Lamping, N., Müller, J., Esper, O., Hillenbrand, C., Smith, J. A., and Kuhn, G.: Highly branched isoprenoids reveal onset of deglaciation followed by dynamic sea-ice conditions in the western Amundsen Sea, Antarctica, *Quaternary Sci. Rev.*, 228, 106103, <https://doi.org/10.1016/j.quascirev.2019.106103>, 2020.
- Lamy, F.: The expedition PS97 of the research vessel POLARSTERN to the Drake Passage in 2016, Reports on Polar and Marine Research, Bremerhaven, Germany, 571 pp., [https://doi.org/10.2312/BzPM\\_0702\\_2016](https://doi.org/10.2312/BzPM_0702_2016), 2016.
- Leventer, A.: The fate of Antarctic “sea ice diatoms” and their use as paleoenvironmental indicators, American Geophysical Union, in: Antarctic Sea Ice: Biological Processes, Interactions and Variability, edited by: Lizotte, M. P. and Arrigo, K. R., 73, 121–137, <https://doi.org/10.1029/AR073>, 1998.
- Li, J., Xie, S.-P., Cook, E. R., Morales, M. S., Christie, D. A., Johnson, N. C., Chen, F., D’Arrigo, R., Fowler, A. M., Gou, X., and Fang, K.: El Niño modulations over the past seven centuries, *Nat. Clim. Change*, 3, 822–826, <https://doi.org/10.1038/nclimate1936>, 2013.
- Liu, J., Curry, J. A., and Martinson, D. G.: Interpretation of recent Antarctic sea ice variability, *Geophys. Res. Lett.*, 31, 2000–2003, <https://doi.org/10.1029/2003GL018732>, 2004.
- Liu, X.-L., Lipp, J. S., Simpson, J. H., Lin, Y.-S., Summons, R. E., and Hinrichs, K.-U.: Mono- and dihydroxyl glycerol dibiphytanyl glycerol tetraethers in marine sediments: Identification of both core and intact polar lipid forms, *Geochim. Cosmochim. Ac.*, 89, 102–115, <https://doi.org/10.1016/j.gca.2012.04.053>, 2012.
- Lorenz, S. J. and Lohmann, G.: Acceleration technique for Milankovitch type forcing in a coupled atmosphere-ocean circulation model: Method and application for the Holocene, *Clim. Dynam.*, 23, 727–743, <https://doi.org/10.1007/s00382-004-0469-y>, 2004.
- Lü, X., Liu, X. L., Elling, F. J., Yang, H., Xie, S., Song, J., Li, X., Yuan, H., Li, N., and Hinrichs, K. U.: Hydroxylated isoprenoid GDGTs in Chinese coastal seas and their potential as a paleotemperature proxy for mid-to-low latitude marginal seas, *Org. Geochem.*, 89/90, 31–43, <https://doi.org/10.1016/j.orggeochem.2015.10.004>, 2015.
- Marshall, G. J., Orr, A., van Lipzig, N. P. M. and King, J. C.: The Impact of a Changing Southern Hemisphere Annular Mode on Antarctic Peninsula Summer Temperatures, *J. Climate*, 19, 5388–5404, <https://doi.org/10.1175/JCLI3844.1>, 2006.
- Martinson, D. G. and McKee, D. C.: Transport of warm Upper Circumpolar Deep Water onto the western Antarctic Peninsula continental shelf, *Ocean Sci.*, 8, 433–442, <https://doi.org/10.5194/os-8-433-2012>, 2012.
- Massé, G., Belt, S. T., Crosta, X., Schmidt, S., Snape, I., Thomas, D. N., and Rowland, S. J.: Highly branched isoprenoids as proxies for variable sea ice conditions in the Southern Ocean, *Antarct. Sci.*, 23, 487–498, <https://doi.org/10.1017/S0954102011000381>, 2011.

- Meijers, A. J. S., Meredith, M. P., Abrahamsen, E. P., Morales Maqueda, M. A., Jones, D. C., and Naveira Garabato, A. C.: Wind-driven export of Weddell Sea slope water, *J. Geophys. Res.-Oceans*, 121, 7530–7546, <https://doi.org/10.1002/2016JC011757>, 2016.
- Meinshausen, M., Smith, S. J., Calvin, K., Daniel, J. S., Kainuma, M. L. T., Lamarque, J.-F., Matsumoto, K., Montzka, S. A., Raper, S. C. B., Riahi, K., Thomson, A., Velders, G. J. M., and van Vuuren, D. P. P.: The RCP greenhouse gas concentrations and their extensions from 1765 to 2300, *Climatic Change*, 109, 213–241, <https://doi.org/10.1007/s10584-011-0156-z>, 2011.
- Meinshausen, M., Vogel, E., Nauels, A., Lorbacher, K., Meinshausen, N., Etheridge, D. M., Fraser, P. J., Montzka, S. A., Rayner, P. J., Trudinger, C. M., Krummel, P. B., Beyerle, U., Canadell, J. G., Daniel, J. S., Enting, I. G., Law, R. M., Lunder, C. R., O'Doherty, S., Prinn, R. G., Reimann, S., Rubino, M., Velders, G. J. M., Vollmer, M. K., Wang, R. H. J., and Weiss, R.: Historical greenhouse gas concentrations for climate modelling (CMIP6), *Geosci. Model Dev.*, 10, 2057–2116, <https://doi.org/10.5194/gmd-10-2057-2017>, 2017.
- Meredith, M. P. and King, J. C.: Rapid climate change in the ocean west of the Antarctic Peninsula during the second half of the 20th century, *Geophys. Res. Lett.*, 32, 1–5, <https://doi.org/10.1029/2005GL024042>, 2005.
- Meredith, M. P., Falk, U., Bers, A. V., Mackensen, A., Schloss, I. R., Barlett, E. R., Jerosch, K., Busso, A. S., and Abele, D.: Anatomy of a glacial meltwater discharge event in an Antarctic cove, *Philos. T. Roy. Soc. A*, 376, 20170163, <https://doi.org/10.1098/rsta.2017.0163>, 2018.
- Moffat, C. and Meredith, M.: Shelf-ocean exchange and hydrography west of the Antarctic Peninsula: A review, *Philos. T. Roy. Soc. A*, 376, 20170164, <https://doi.org/10.1098/rsta.2017.0164>, 2018.
- Montes-Hugo, M., Doney, S. C., Ducklow, H. W., Fraser, W., Martinson, D., Stammerjohn, S. E., and Schofield, O.: Recent Changes in Phytoplankton Communities Associated with Rapid Regional Climate Change Along the Western Antarctic Peninsula, *Science*, 323, 1470–1473, <https://doi.org/10.1126/science.1164533>, 2009.
- Müller, J., Wagner, A., Fahl, K., Stein, R., Prange, M., and Lohmann, G.: Towards quantitative sea ice reconstructions in the northern North Atlantic: A combined biomarker and numerical modelling approach, *Earth Planet. Sci. Lett.*, 306, 137–148, <https://doi.org/10.1016/J.EPSL.2011.04.011>, 2011.
- Müller, J., Werner, K., Stein, R., Fahl, K., Moros, M., and Jansen, E.: Holocene cooling culminates in sea ice oscillations in Fram Strait, *Quaternary Sci. Rev.*, 47, 1–14, <https://doi.org/10.1016/j.quascirev.2012.04.024>, 2012.
- Nicholls, K. W., Østerhus, S., Makinson, K., Gammelsrød, T., and Fahrbach, E.: Ice-ocean processes over the continental shelf of the southern Weddell Sea, Antarctica: A review, *Rev. Geophys.*, 47, RG3003, <https://doi.org/10.1029/2007RG000250>, 2009.
- Nichols, P. D., Volkman, J. K., Palmisano, A. C., Smith, G. A., and White, D. C.: Occurrence of an Isoprenoid C<sub>25</sub> diunsaturated alkene and high neutral lipid content in Antarctic Sea-Ice Diatom communities, *J. Phycol.*, 24, 90–96, 1988.
- Oksanen, J., Blanchet, F. G., Kindt, R., Legendre, P., Minchin, P. R., O'Hara, R. B., Simpson, G. L., Solymos, P., Stevens, M. H. H., and Wagner, H.: Vegan: Community Ecology Package (R Package Version 2.0-3), available at: <http://cran.r-project.org/> (last access: 24 March 2020), 2012.
- Otto-Bliesner, B. L., Braconnot, P., Harrison, S. P., Lunt, D. J., Abe-Ouchi, A., Albani, S., Bartlein, P. J., Capron, E., Carlson, A. E., Dutton, A., Fischer, H., Goelzer, H., Govin, A., Haywood, A., Joos, F., LeGrande, A. N., Lipscomb, W. H., Lohmann, G., Mahowald, N., Nehrbass-Ahles, C., Pausata, F. S. R., Peterschmitt, J.-Y., Phipps, S. J., Renssen, H., and Zhang, Q.: The PMIP4 contribution to CMIP6 – Part 2: Two interglacials, scientific objective and experimental design for Holocene and Last Interglacial simulations, *Geosci. Model Dev.*, 10, 3979–4003, <https://doi.org/10.5194/gmd-10-3979-2017>, 2017.
- Palanques, A., Isla, E., Puig, P., Sanchez-Cabeza, J. A., and Masqué, P.: Annual evolution of downward particle fluxes in the Western Bransfield Strait (Antarctica) during the FRUELA project, *Deep Sea Research Part II: Topical Studies in Oceanography*, 49, 903–920, [https://doi.org/10.1016/S0967-0645\(01\)00130-8](https://doi.org/10.1016/S0967-0645(01)00130-8), 2002.
- Park, E., Hefter, J., Fischer, G., Iversen, M. H., Ramondenc, S., Nöthig, E.-M., and Mollenhauer, G.: Seasonality of archaeal lipid flux and GDGT-based thermometry in sinking particles of high-latitude oceans: Fram Strait (79°N) and Antarctic Polar Front (50°S), *Biogeosciences*, 16, 2247–2268, <https://doi.org/10.5194/bg-16-2247-2019>, 2019.
- Parkinson, C. L.: Trends in the length of the Southern Ocean sea-ice season, 1979–99, *Ann. Glaciol.*, 34, 435–440, <https://doi.org/10.3189/172756402781817482>, 2002.
- Parkinson, C. L.: A 40-y record reveals gradual Antarctic sea ice increases followed by decreases at rates far exceeding the rates seen in the Arctic, *P. Natl. Acad. Sci.*, 116, 14414–14423, <https://doi.org/10.1073/pnas.1906556116>, 2019.
- Parkinson, C. L. and Cavalieri, D. J.: Antarctic sea ice variability and trends, 1979–2010, *The Cryosphere*, 6, 871–880, <https://doi.org/10.5194/tc-6-871-2012>, 2012.
- Peltier, W. R., Argus, D. F., and Drummond, R.: Space geodesy constrains ice age terminal deglaciation: The global ICE-6G\_C (VM5a) model, *J. Geophys. Res.-Sol. Ea.*, 120, 450–487, <https://doi.org/10.1002/2014JB011176>, 2015.
- Pisias, N. G. and Mix, A. C.: Aliasing of the geologic record and the search for long-period Milankovitch cycles, *Paleoceanography*, 3, 613–619, <https://doi.org/10.1029/PA003i005p00613>, 1988.
- Porter, S. E., Parkinson, C. L., and Mosley-Thompson, E.: Bellingshausen Sea ice extent recorded in an Antarctic Peninsula ice core, *J. Geophys. Res.-Atmos.*, 121, 886–900, <https://doi.org/10.1002/2016JD025626>, 2016.
- QGIS: QGIS Geographic Information System, available at: <http://qgis.osgeo.org> (last access: 26 March 2020), 2018.
- Raddatz, T. J., Reick, C. H., Knorr, W., Kattge, J., Roeckner, E., Schnur, R., Schnitzler, K. G., Wetzell, P., and Jungclaus, J.: Will the tropical land biosphere dominate the climate-carbon cycle feedback during the twenty-first century?, *Clim. Dynam.*, 29, 565–574, <https://doi.org/10.1007/s00382-007-0247-8>, 2007.
- Ragueneau, O., Tréguer, P., Leynaert, A., Anderson, R. F., Brzezinski, M. A., DeMaster, D. J., Dugdale, R. C., Dymond, J., Fischer, G., François, R., Heinze, C., Maier-Reimer, E., Martin-Jézéquel, V., Nelson, D. M., and Quéguiner, B.: A review of the Si cycle in the modern ocean: recent progress and missing gaps in the application of biogenic opal as a paleoproductivity proxy, *Global Planet. Change*, 26, 317–365, [https://doi.org/10.1016/S0921-8181\(00\)00052-7](https://doi.org/10.1016/S0921-8181(00)00052-7), 2000.

- Rahaman, W., Chatterjee, S., Ejaz, T., and Thamban, M.: Increased influence of ENSO on Antarctic temperature since the Industrial Era, *Sci. Rep.-UK*, 9, 6006, <https://doi.org/10.1038/s41598-019-42499-x>, 2019.
- R Core Team: a Language and Environment for Statistical Computing, R Foundation for Statistical computing, Vienna, available at: <http://cran.r-project.org/> (last access: 24 March 2020) 2012.
- Reynolds, R. W., Rayner, N. A., Smith, T. M., Stokes, D. C., and Wang, W.: An Improved In Situ and Satellite SST Analysis for Climate, *J. Climate*, 15, 1609–1625, [https://doi.org/10.1175/1520-0442\(2002\)015<1609:AISAS>2.0.CO;2](https://doi.org/10.1175/1520-0442(2002)015<1609:AISAS>2.0.CO;2), 2002.
- Reynolds, R. W., Smith, T. M., Liu, C., Chelton, D. B., Casey, K. S., Schlax, M. G., Reynolds, R. W., Smith, T. M., Liu, C., Chelton, D. B., Casey, K. S., and Schlax, M. G.: Daily High-Resolution-Blended Analyses for Sea Surface Temperature, *J. Climate*, 20, 5473–5496, <https://doi.org/10.1175/2007JCLI1824.1>, 2007.
- Riaux-Gobin, C. and Poulin, M.: Possible symbiosis of *Berkeleya adeliensis* Medlin, *Synedropsis fragilis* (Manguin) Hasle et al.: *Nitzschia lecontei* Van Heurck (bacillariophyta) associated with land-fast ice in Adélie Land, Antarctica, *Diatom Res.*, 19, 265–274, <https://doi.org/10.1080/0269249X.2004.9705874>, 2004.
- Rignot, E., Mouginot, J., Scheuchl, B., van den Broeke, M., van Wessem, M. J., and Morlighem, M.: Four decades of Antarctic Ice Sheet mass balance from 1979–2017, *P. Natl. Acad. Sci.*, 116, 1095–1103, <https://doi.org/10.1073/pnas.1812883116>, 2019.
- Rontani, J. F., Belt, S. T., Vaultier, F., and Brown, T. A.: Visible light induced photo-oxidation of highly branched isoprenoid (HBI) alkenes: Significant dependence on the number and nature of double bonds, *Org. Geochem.*, 42, 812–822, <https://doi.org/10.1016/j.orggeochem.2011.04.013>, 2011.
- Rontani, J.-F., Charriere, B., Petit, M., Vaultier, F., Heipieper, H. J., Link, H., Chaillou, G., and Sempéré, R.: Degradation state of organic matter in surface sediments from the Southern Beaufort Sea: a lipid approach, *Biogeosciences*, 9, 3513–3530, <https://doi.org/10.5194/bg-9-3513-2012>, 2012.
- Rontani, J.-F., Belt, S. T., Vaultier, F., Brown, T. A., and Massé, G.: Autoxidative and Photooxidative Reactivity of Highly Branched Isoprenoid (HBI) Alkenes, *Lipids*, 49, 481–494, <https://doi.org/10.1007/s11745-014-3891-x>, 2014.
- Rontani, J., Smik, L., and Belt, S. T.: Autoxidation of the sea ice biomarker proxy IPSO25 in the near-surface oxic layers of Arctic and Antarctic sediments, *Org. Geochem.*, 129, 63–76, <https://doi.org/10.1016/J.ORGGEOCHEM.2019.02.002>, 2019.
- Rosenblum, E. and Eisenman, I.: Sea Ice Trends in Climate Models Only Accurate in Runs with Biased Global Warming, *J. Climate*, 30, 6265–6278, <https://doi.org/10.1175/JCLI-D-16-0455.1>, 2017.
- Ruiz Barlett, E. M., Tosonotto, G. V., Piola, A. R., Sierra, M. E., and Mata, M. M.: On the temporal variability of intermediate and deep waters in the Western Basin of the Bransfield Strait, *Deep Sea Research Part II: Topical Studies in Oceanography*, 149, 31–46, <https://doi.org/10.1016/j.dsr2.2017.12.010>, 2018.
- Sanchez, N., Reiss, C. S., Holm-Hansen, O., Hewes, C. D., Bizsel, K. C., and Ardelan, M. V.: Weddell-Scotia Confluence Effect on the Iron Distribution in Waters Surrounding the South Shetland (Antarctic Peninsula) and South Orkney (Scotia Sea) Islands During the Austral Summer in 2007 and 2008, *Frontiers Mar. Sci.*, 6, 1–16, <https://doi.org/10.3389/fmars.2019.00771>, 2019.
- Sanchez-Cabeza, J.-A., Ruiz-Fernández, A. C., Ontiveros-Cuadras, J. F., Pérez Bernal, L. H., and Olid, C.: Monte Carlo uncertainty calculation of  $^{210}\text{Pb}$  chronologies and accumulation rates of sediments and peat bogs, *Quat. Geochronol.*, 23, 80–93, <https://doi.org/10.1016/J.QUAGEO.2014.06.002>, 2014.
- Sangrà, P., Gordo, C., Hernández-Arencibia, M., Marrero-Díaz, A., Rodríguez-Santana, A., Stegner, A., Martínez-Marrero, A., Pelegrí, J. L., and Pichon, T.: The Bransfield current system, *Deep Sea Research Part I: Oceanographic Research Papers*, 58, 390–402, <https://doi.org/10.1016/J.DSR.2011.01.011>, 2011.
- Sangrà, P., Stegner, A., Hernández-Arencibia, M., Marrero-Díaz, Á., Salinas, C., Aguiar-González, B., Henríquez-Pastene, C., and Mouriño-Carballido, B.: The Bransfield Gravity Current, *Deep-Sea Research Part I: Oceanographic Research Papers*, 119, 1–15, <https://doi.org/10.1016/j.dsr.2016.11.003>, 2017.
- Schofield, O., Brown, M., Kohut, J., Nardelli, S., Saba, G., Waite, N., and Ducklow, H.: Changes in the upper ocean mixed layer and phytoplankton productivity along the West Antarctic Peninsula, *Philos. T. Roy. Soc. A*, 376, <https://doi.org/10.1098/rsta.2017.0173>, 2018.
- Schouten, S., Hopmans, E. C., and Sinninghe Damsté, J. S.: The organic geochemistry of glycerol dialkyl glycerol tetraether lipids: A review, *Org. Geochem.*, 54, 19–61, <https://doi.org/10.1016/j.orggeochem.2012.09.006>, 2013.
- Schrader, H. and Gersonde, R.: Diatoms and silicoflagellates, in: *Utrecht Micropaleontological Bulletins*, 17, 129–176., 1978.
- Shi, X. and Lohmann, G.: Simulated response of the mid-Holocene Atlantic meridional overturning circulation in ECHAM6-FESOM/MPIOM, *J. Geophys. Res.-Oceans*, 121, 6444–6469, <https://doi.org/10.1002/2015JC011584>, 2016.
- Shi, X., Lohmann, G., Sidorenko, D., and Yang, H.: Early-Holocene simulations using different forcings and resolutions in AWI-ESM, *Holocene*, 30, 996–1015, <https://doi.org/10.1177/0959683620908634>, 2020.
- Sidorenko, D., Goessling, H. F., Koldunov, N. V., Scholz, P., Danilov, S., Barbi, D., Cabos, W., Gurses, O., Harig, S., Hinrichs, C., Juricke, S., Lohmann, G., Losch, M., Mu, L., Rackow, T., Rakowsky, N., Sein, D., Semmler, T., Shi, X., Stepanek, C., Streffing, J., Wang, Q., Wekerle, C., Yang, H., and Jung, T.: Evaluation of FESOM2.0 coupled to ECHAM6.3: Pre-industrial and HighResMIP simulations, *J. Adv. Model. Earth Sy.*, 2019MS001696, <https://doi.org/10.1029/2019MS001696>, 2019.
- Simpson, G. L. and Oksanen, J.: Analogue: Analogue Matching and Modern Analogue Technique Transfer Function Models, R Package Version 0.8-2, available at: <http://cran.r-project.org/> (last access: 24 March 2020), 2012.
- Sinninghe Damsté, J. S., Rijpstra, W. I. C., Coolen, M. J. L., Schouten, S., and Volkman, J. K.: Rapid sulfurisation of highly branched isoprenoid (HBI) alkenes in sulfidic Holocene sediments from Ellis Fjord, Antarctica, *Org. Geochem.*, 38, 128–139, <https://doi.org/10.1016/j.orggeochem.2006.08.003>, 2007.
- Smik, L., Belt, S. T., Lieser, J. L., Armand, L. K., and Leventer, A.: Distributions of highly branched isoprenoid alkenes and other algal lipids in surface waters from East Antarctica: Further insights for biomarker-based paleo sea-ice reconstruction, *Org. Geochem.*, 95, 71–80, <https://doi.org/10.1016/J.ORGGEOCHEM.2016.02.011>, 2016a.
- Smik, L., Cabedo-Sanz, P., and Belt, S. T.: Semi-quantitative estimates of paleo Arctic sea ice concentration based on source-

- specific highly branched isoprenoid alkenes: A further development of the PIP 25 index, *Org. Geochem.*, 92, 63–69, <https://doi.org/10.1016/j.orggeochem.2015.12.007>, 2016b.
- Stammerjohn, S. E., Martinson, D. G., Smith, R. C., and Iannuzzi, R. A.: Sea ice in the western Antarctic Peninsula region: Spatio-temporal variability from ecological and climate change perspectives, *Deep-Sea Research Part II: Topical Studies in Oceanography*, 55, 2041–2058, <https://doi.org/10.1016/j.dsr2.2008.04.026>, 2008a.
- Stammerjohn, S. E., Martinson, D. G., Smith, R. C., Yuan, X., and Rind, D.: Trends in Antarctic annual sea ice retreat and advance and their relation to El Niño – Southern Oscillation and Southern Annular Mode variability, *J. Geophys. Res.*, 113, C03S90, <https://doi.org/10.1029/2007JC004269>, 2008b.
- Stastna, V.: Spatio-temporal changes in surface air temperature in the region of the northern Antarctic Peninsula and south Shetland islands during 1950–2003, *Polar Sci.*, 4, 18–33, <https://doi.org/10.1016/j.polar.2010.02.001>, 2010.
- Stein, R., Fahl, K., and Müller, J.: Proxy Reconstruction of Cenozoic Arctic Ocean Sea-Ice History: from IRD to IP25, *Polarforschung*, 82, 37–71, 2012.
- Stevens, B., Giorgetta, M., Esch, M., Mauritsen, T., Crueger, T., Rast, S., Salzmann, M., Schmidt, H., Bader, J., Block, K., Brokopf, R., Fast, I., Kinne, S., Kornblueh, L., Lohmann, U., Pincus, R., Reichler, T., and Roeckner, E.: Atmospheric component of the MPI-M Earth System Model: ECHAM6, *J. Adv. Model. Earth Sy.*, 5, 146–172, <https://doi.org/10.1002/jame.20015>, 2013.
- Tans, P. and Keeling, R.: Trends in Atmospheric Carbon Dioxide, Mauna Loa CO<sub>2</sub> annual mean data, available at: <https://www.esrl.noaa.gov/gmd/ccgg/trends/>, last access: 7 August 2020.
- Taylor, F., Whitehead, J., and Domack, E.: Holocene paleoclimate change in the Antarctic Peninsula: Evidence from the diatom, sedimentary and geochemical record, *Mar. Micropaleontol.*, 41, 25–43, [https://doi.org/10.1016/S0377-8398\(00\)00049-9](https://doi.org/10.1016/S0377-8398(00)00049-9), 2001.
- Thomas, E. R., Allen, C. S., Etourneau, J., King, A. C. F., Severi, M., Winton, V. H. L., Müller, J., Crosta, X., and Peck, V. L.: Antarctic Sea Ice Proxies from Marine and Ice Core Archives Suitable for Reconstructing Sea Ice over the past 2000 Years, *Geosciences*, 9, 506, <https://doi.org/10.3390/geosciences9120506>, 2019.
- Trevena, A. J. and Jones, G. B.: Dimethylsulphide and dimethylsulphoniopropionate in Antarctic sea ice and their release during sea ice melting, *Mar. Chem.*, 98, 210–222, <https://doi.org/10.1016/j.marchem.2005.09.005>, 2006.
- Turner, J., Orr, A., Gudmundsson, G. H., Jenkins, A., Bingham, R. G., Hillenbrand, C.-D., and Bracegirdle, T. J.: Atmosphere-ocean-ice interactions in the Amundsen Sea Embayment, West Antarctica, *Rev. Geophys.*, 55, 235–276, <https://doi.org/10.1002/2016RG000532>, 2017.
- Turner, J., Marshall, G. J., Clem, K., Colwell, S., Phillips, T., and Lu, H.: Antarctic temperature variability and change from station data, *Int. J. Climatol.*, 40, 2986–3007, <https://doi.org/10.1002/joc.6378>, 2019.
- Vaughan, D. G., Marshall, G. J., Connolley, W. M., Parkinson, C., Mulvaney, R., Hodgson, D. A., King, J. C., Pudsey, C. J., and Turner, J.: Recent Rapid Regional Climate Warming on the Antarctic Peninsula, *Clim. Change*, 60, 243–274, <https://doi.org/10.1023/A:1026021217991>, 2003.
- Vernet, M., Martinson, D., Iannuzzi, R., Stammerjohn, S., Kozłowski, W., Sines, K., Smith, R., and Garibotti, I.: Primary production within the sea-ice zone west of the Antarctic Peninsula: I – Sea ice, summer mixed layer, and irradiance, *Deep Sea Research Part II: Topical Studies in Oceanography*, 55, 2068–2085, <https://doi.org/10.1016/j.dsr2.2008.05.021>, 2008.
- Volkman, J. K.: A review of sterol markers for marine and terrigenous organic matter, *Org. Geochem.*, 9, 83–99, [https://doi.org/10.1016/0146-6380\(86\)90089-6](https://doi.org/10.1016/0146-6380(86)90089-6), 1986.
- Vorrath, M.-E., Müller, J., Esper, O., Mollenhauer, G., Haas, C., Schefuß, E., and Fahl, K.: Highly branched isoprenoids for Southern Ocean sea ice reconstructions: a pilot study from the Western Antarctic Peninsula, *Biogeosciences*, 16, 2961–2981, <https://doi.org/10.5194/bg-16-2961-2019>, 2019.
- Vorrath, M.-E., Müller, J., Rebolledo, L., Cárdenas, P., Shi, X., Esper, O., Opel, T., Geibert, W., Muñoz, P., Haas, C., Lange, C. B., Lohmann, G., and Mollenhauer, G.: Sea Ice dynamics in the Bransfield Strait, Antarctic Peninsula, during the past 240 years: a multi-proxy intercomparison study, <https://doi.org/10.1594/PANGAEA.918808>, Pangaea, 2020.
- Wang, J.-X., Wei, Y., Wang, P., Hong, Y., and Zhang, C. L.: Unusually low TEX<sub>86</sub> values in the transitional zone between Pearl River estuary and coastal South China Sea: Impact of changing archaeal community composition, *Chem. Geol.*, 402, 18–29, <https://doi.org/10.1016/j.chemgeo.2015.03.002>, 2015.
- Wefer, G., Fischer, G., Fuetterer, D., and Gersonde, R.: Seasonal particle flux in the Bransfield Strait, Antarctica, *Deep Sea Research Part A. Oceanographic Research Papers*, 35, 891–898, [https://doi.org/10.1016/0198-0149\(88\)90066-0](https://doi.org/10.1016/0198-0149(88)90066-0), 1988.
- Wu, S., Kuhn, G., Diekmann, B., Lembke-Jene, L., Tiedemann, R., Zheng, X., Ehrhardt, S., Arz, H. W., and Lamy, F.: Surface sediment characteristics related to provenance and ocean circulation in the Drake Passage sector of the Southern Ocean, *Deep Sea Research Part I: Oceanographic Research Papers*, 154, 103135, <https://doi.org/10.1016/j.dsr.2019.103135>, 2019.
- Xiao, X., Fahl, K., and Stein, R.: Biomarker distributions in surface sediments from the Kara and Laptev seas (Arctic Ocean): indicators for organic-carbon sources and sea-ice coverage, *Quaternary Sci. Rev.*, 79, 40–52, <https://doi.org/10.1016/j.quascirev.2012.11.028>, 2013.
- Yuan, X.: ENSO-related impacts on Antarctic sea ice: a synthesis of phenomenon and mechanisms, *Antarct. Sci.*, 16, 415–425, <https://doi.org/10.1017/S0954102004002238>, 2004.
- Zhou, M., Niiler, P. P., and Hu, J. H.: Surface currents in the Bransfield and Gerlache Straits, Antarctica, *Deep-Sea Research Part I: Oceanographic Research Papers*, 49, 267–280, [https://doi.org/10.1016/S0967-0637\(01\)00062-0](https://doi.org/10.1016/S0967-0637(01)00062-0), 2002.
- Zwally, H. J., Comiso, J. C., Parkinson, C. L., Cavalieri, D. J., and Gloersen, P.: Variability of Antarctic sea ice 1979–1998, *J. Geophys. Res.*, 107, 3041, <https://doi.org/10.1029/2000JC000733>, 2002.